

Declaration

The present master thesis has been authored by Michael Weber.

It represents a student work, which has been developed under supervision of a scientific staff member at the “Federal Institute for Geosciences and Natural Resources (BGR)” in Hannover. Scientific findings presented in this study are student-based assessments and do not necessarily have to represent the appraisals of the Institute. This report is not a scientific publication and will not be permanently available as source of information.

I hereby declare that this master thesis „Numerical Investigation of Transient Water Flow in the Chtouka Aquifer, Morocco“ is the sole result of my independent research except where indicated by references to other sources and bibliography of other authors or by assistance of any kind. This study has not been presented to the Examination Authority or been published so far. I am aware that a false statement will have legal consequences.

Hannover, 06.10.2022

Contents

List of Figures	iii
List of Tables	iv
List of Abbreviations	vi
Nomenclature	viii
1 Introduction	1
1.0.1 Relevance of Groundwater Resources	1
1.0.2 Seawater Intrusion	2
1.0.3 The need for modelling of coastal aquifers	2
1.0.4 Specification of this study	3
1.0.5 Specification to the Modelling conducted in this Work, regarding the Chtouka Aquifer in Morocco	4
2 Theoretical Background	7
2.1 Fundamental Terms	7
2.2 The Groundwater Flow Equation	8
3 Study Region: The Chtouka-Massa Plain	11
3.1 Localisation	11
3.2 (Hydro)Geology	12
3.3 Climate	13
3.4 Structure of the Region	15
3.5 Hydrology	16
3.6 Unused Additional Information	19
4 Conceptual Model/Model Geometry	23
4.1 (Horizontal) Delineation of the Model	23
4.1.1 Northern Boundary	23
4.1.2 Eastern Boundary	24
4.1.3 Southern Boundary	26
4.1.4 Western Boundary	27
4.2 Geological Model	27
4.3 Recharge from Precipitation	29

4.4	Groundwater Wells	29
4.4.1	Drinking Wells	30
4.4.2	Irrigation Wells	30
4.5	Irrigation Returns	31
4.6	Observations	31
5	Implementation of the Model	37
5.1	Implementation of the Model	37
5.1.1	Modelling Software: GMS	37
5.1.2	Model Equations	38
5.1.3	Implementation in GMS	38
5.1.4	Discretisation	39
5.2	Methodology of Sensitivity Analysis and Calibration	41
5.2.1	Examined Parameters	43
5.2.2	Methodology of the Sensitivity Analysis	45
5.2.3	Methodology of the Calibration	46
5.2.4	Error Assessment	47
6	Results	53
6.1	Discussion of Error Measure	53
6.2	Sensitivity Analysis	54
6.2.1	Calibration	56
6.2.2	1-2	58
6.3	2	59
6.3.1	2-1	59
7	Summary and Discussion	61
Bibliography		63
A	Task of the Master Thesis	67

List of Figures

1.1	Figure Example	5
3.1	Map of the Souss-Massa basin, which contains the Chtouka aquifer. This representation was derived from digital elevation model data of NASA JPL, 2013 and follows in topographical colouring Hssaisoune et al., 2017.	12
3.2	Climatic conditions in the Chtouka-Massa plain. (a): Annual precipitations at the city of Biougra in the period 1970 to 2016. Measured are the respective hydrological years, from 1st of September of the denoted year to 31st of August of the following year. The underlying dataset was provided by the ABHSMD. (b): Long-term average temperatures and precipitation during a year. The climate chart bases on data for the years 1950-2017 and is derived from the gridded monthly time series datasets Matsuura and Willmott, 2018a and Matsuura and Willmott, 2018b.	14
3.3	A Map showing the Chtouka-Massa plain in the Souss Massa River Basin. The map is derived from the digital elevation model data of NASA JPL, 2013 accessed through USGS, 2018. [To be revised: name of channel, representation of water bodies: main oueds and intermittent oueds, different colouring of agri-perimeters, "cities" renamed to "municipalities", adding of $i=2$ more cities: Sidi Bibi and one on eastern boundary; north arrow same colouring as scale;...?]	20
3.4	Photograph of the YBT dam. [could be deleted, as not really necessary; would only add a nice picture to the text]	21
4.1	The water balance of the system. [Arrows and labels will be revised to look better, as well as the cloud for precipitation]	24
4.2	The delineated modelling area of the Chtouka aquifer. Shown are the four differently characterised boundaries (Section 4.1), the three different precipitation zones (Section ??) and the piezometers that are used for definition of the eastern boundary with differentiation between piezometers providing single point-in-time (PiT) and time series (TS) measurements (Section 4.1), as well as the piezometers for the model evaluation (Section 4.6). [adjust: background of prec-zones; instead: black line: boundaries of precipitation zones.]	33

4.3	The adjusted Dirichlet boundary condition for the eastern boundary. The for 1968 estimated initial head (thick blue line) along with the bottom- (thick black dotted) and surface- (thick black dashed) elevations are shown at the starting year 1968. Measured heads are shown in red as circles for single point-in-time (PiT) measurements and as triangles for time series (TS) measurements. The grid (blue) spanning the temporal evolution of heads shows the linear interpolation in between the 29 locations and the five specified years. For better perceptability the surface marking the head stages in between these points is coloured according to head values.	34
4.4	[Representation will be similar to the one from Horn, 2021, Fig. 5.1] The already discretised geological model of the Chtouka Aquifer, as defined by Horn, 2021. (a) presents a 3D view, with the black line denoting the crossection shown in (b). It uses the chosen horizontal grid resolution of 500 m × 500 m and 10 equally spaced layers in z-direction (see Section 5.1.4). The xy -plane is oriented along the four cardinal directions with the positive x -direction pointing to the north. For presentation purposes, a z -magnification with a factor of 10 is applied.	35
4.5	Time series of annual groundwater recharge in the three different zones (Figure 4.2) as identified by Horn, 2021.	35
4.6	Spatial distribution of the in this study considered 650 drinking wells (a) and 5498 irrigation wells. In (b) a distinction between wells from the two different surveys from 2003 (green) and 2015 (red) is made.	36
5.1	Example of a two dimensional continuous parameter space Θ with ele- ments $\boldsymbol{\theta} = (\theta_{1,i}, \theta_{2,j})$. Each of these parameter sets corresponds to an ab- solute modelling error δ_{SM} marked by the colour scale. In this example, the parameter set $\boldsymbol{\theta}_{lo}$ corresponds to a local minimum of the modelling error δ_{SM} . The global optimum of δ_{SM} is obtained by the parameter set $\boldsymbol{\theta}_{go}$	42
5.2	(a): Time series of an observation and of three simulations with different parameter sets. In comparison with the observation all three simulations have an equal $RMSE$. (b): Linear representation of the correlations between observed and simulated heads for the three simulations from (a). The respective data sets are each fitted with a linear (lin.) regression. The black dashed line marks identity between observed and simulated head.	50
6.1	Figure example.	58
6.2	Figure Example.	59

List of Tables

List of Abbreviations

GMS	-	Groundwater Modeling System
MAE	-	mean average error
RMSE	-	root mean squared error
TIN	-	triangulated irregular network
YBT	-	Youssef Ben Tachfine
PiT	-	point-in-time
TS	-	time series
calc.	-	calcareous
lin.	-	linear
m.a.s.l.	-	meter above sea level

a

optionals:

MODFLOW		
MT3DMS	-	Modular Transport, 3-Dimensional, Multi-Species model
SEAWAT	-	
GPS	-	Global Positioning System

Nomenclature

[use classification into Latin and Greek symbols]

f	-	function
\mathbf{X}	-	key variable
\mathbf{x}	-	key variable

T	-	truth
S	-	simulation result
M	-	analytical modelling result
E	-	measurement result
δ_E	-	measurement error
δ_{SM}	-	simulation modelling error
δ_{SN}	-	simulation numerical error
δ_E	-	measurement error
$\boldsymbol{\theta}$	-	parameter set
θ	-	parameter value
Θ	-	parameter space
S_s	-	specific storage
S_y	-	specific yield
K	-	hydraulic conductivity
K_h	-	horizontal hydraulic conductivity
K_v	-	vertical hydraulic conductivity
ϕ	-	porosity
V_p	-	pore volume
V_{tot}	-	total volume
ϕ_{eff}	-	effective porosity
V_w	-	water volume
$V_{w,g}$	-	volume of gravity groundwater
S	-	storativity
b	-	aquifer thickness
A	-	area
h	-	head
C	-	conductance
k	-	hydraulic conductivity
t	-	riverbed thickness
w	-	riverbed width
W	-	source- and sink-term
t	-	time
i	-	index
j	-	index

Chapter 1

Introduction

1.0.1 Relevance of Groundwater Resources

what to include:

- Groundwater as fresh water source in many, especially arid and semi-arid regions for drinking and agricultural usage
- intensification of water usage through intensification of agricultural activities (industrialised agriculture) and population growth
- drawdown through over-usage
- drying out of wells, thus necessity of deeper wells (ultimately overexploitation of water resources)
- (plant accessible ground water only in 30 cm to X m below ground, so often in these regions of no importance)
- controlled water deficit irrigation (English, 1990) as possibility for water scarcity/climate change mitigation (what is that? -*i*, explain:
 - deficit irrigation means an irrigation technique, where a lesser amount of water than the optimal amount is given to plants
 - even though this induces a stress in the plants and leads to a reduced crop yield, with the same volume of water over a complete field an over all higher productivity can be achieved (more plants with reduced yield vs. less plants with optimal yield, non-linearity of the crop-water production function)
 - for this irrigation technique to yield proper results, an optimised irrigation schedule is required that allows the crops to "sustain an acceptable degree of water deficit and yield reduction" (Schütze et al., 2012)

1.0.2 Seawater Intrusion

what to include:

- general description of equilibrium between fresh and salt water in coastal areas
- drawdown of fresh ground water levels leads to disturbance of this natural equilibrium and therefore a shift of the fresh water-salt water boundary further inland
- this boundary is however not a sharp boundary, but rather characterised by a continuous mixing and therefore a gradual increase of salinity from the sea side to further inland
- increase of salinity inland leads to salinisation of previously accessed fresh water resources that therefore cannot further be used for drinking or irrigation (at least without desalination)

1.0.3 The need for modelling of coastal aquifers

what to include:

- examples of measures to mitigate water scarcity and saltwater intrusion:
 - reduction of water usage through:
 - * deficit irrigation
 - * more efficient irrigation systems (e.g. drip irrigation instead of sprinklers or flooding)
 - * reduction of tap water usage
 - * more effective water cycles in urban areas
 - * cultivation of different crops with lower water demand
 - * ...?
 - increase of available fresh water resources
 - * operation of desalination plants in coastal areas
 - * import of water from other regions
 - * ...?
 - favourable manipulation of microclimate/microclimatic conditions through changes in land usage

- managemental decisions for or against specific measures highly depend on precise and robust estimations of future water availability and the single measures', site-specific impact on the water resources/water-cycle/...
- these latter impacts, together with different expected outcomes of climate change can be combined to different possible scenarios
- a valuable tool to properly/precisely estimate the impacts of these different scenarios are numerical models of the water system/catchment
- (short explanation of numerical models representing water catchments, leading to specification of this work's model)

1.0.4 Specification of this study

- In this study, the aquifer in the agriculturally important Souss-Massa region in Morocco will be regarded
- as this aquifer is located in coastal central-Morocco, semi-arid climate is present
- fresh water resources are limited to surface water supplied by the neighbouring Youssef Ben Tachfine dam and groundwater
- due to intensive/extensive agricultural activities, the overall water demand exceeds the sustainable supply, which leads to groundwater overexploitation (Choukr-Allah et al., 2017)
- thus, in recent decades large drawdowns of the order of 10^1 m (or: by more than 20 m) can be observed, which lead to (drying out/falling dry) of older wells
- therethrough, the need arises for ever deeper wells, whose construction is associated with significantly higher costs (Quelle?) putting higher pressures on farmers
- furthermore, through these drawdowns of fresh water levels inland, seawater intrusion further inland can be observed (how much?)
- deterioration of groundwater due to saltwater intrusion in coastal areas
- an in a previous study derived numerical steady-state model for the year 1969 in the modelling software GMS will be expanded to simulate ground water flow in transient state
- for the calibration of the model, a newly derived quantification method for the assessment of the yielded results is applied and will be compared to a more simple approach using the root mean square error (RMSE) between observations and simulation results
- ...more?

- state that this study is produced from a cooperation of the Federal Institute for Geosciences and Natural Resources (BGR) and the Agence du Bassin Hydraulique de Souss Massa (et Drâa) (ABHSM(D))

1.0.5 Specification to the Modelling conducted in this Work, regarding the Chtouka Aquifer in Morocco

further notes:

- framework of this study:
 - partnership BGR-OSS
 - CREM-project
 - ...?
- from previous study:
 - steady-state numerical model of the Chtouka Aquifer in Morocco including:
 - geological model
 - delineation of the aquifer
 - identified/modeled/assigned inputs and outputs and their local/spatially resolved (but simplified) modelling
 - * groundwater withdrawal for drinking water
 - * groundwater withdrawal for irrigation
 - * returns from irrigation
 - * delineation of different irrigational areas and their temporal evolution
 - * a
- what has been done within this study/thesis:
 - ...

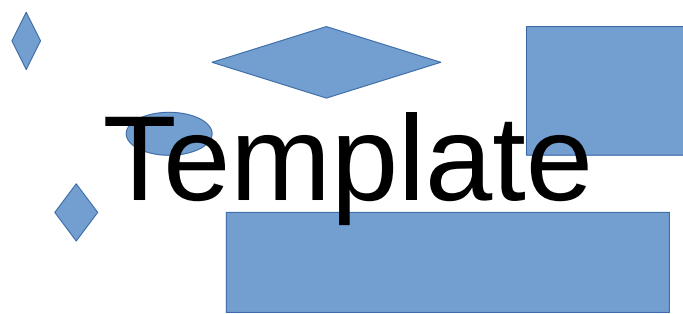


Figure 1.1: Figure Example

Chapter 2

Theoretical Background

2.1 Fundamental Terms

Rocks and soils constituting ground are commonly porous materials, consisting of a solid matrix and an interstitial pore space. Depending on the size of the pores, they can store and conduct groundwater. The ratio between the volume of the pore space V_p and the total volume V_{tot} of a soil probe is called the porosity ϕ (Fetter, 2001),

$$\phi = \frac{V_p}{V_{tot}} \quad (2.1)$$

The accessibility of the pore space to water and to a water flow is limited by the pores of smallest diameter, thus possibly creating non-water filled pores and dead ends. Therefore, only a smaller portion of the pore space is effectively available for groundwater flow. This portion of the pore space is called the effective porosity Φ_{eff} (Fetter, 2001). It is defined as the ratio of the water-accessible volume V_w to the total volume of a soil probe,

$$\Phi_{eff} = \frac{V_w}{V_{tot}} \quad (2.2)$$

On mechanical level, the water contained in a soil interacts with the solid matrix amongst others through molecular and surface tension forces. In case of gravitational drainage of an initially saturated soil, gravitation exerts a stress on the water film enclosing the matrix elements. As the stored water volume decreases, surface tension increases until a balance of the two opposing stresses reaches an equilibrium (Fetter, 2001). The water volume drained through gravitation is called the gravity groundwater, with the corresponding volume being denoted by $V_{W,g}$ (Johnson, 1967). The ratio between $V_{w,g}$ and the total volume V_{tot} is called the specific yield S_y ,

$$S_y = \frac{V_{w,g}}{V_{tot}} \quad (2.3)$$

Another stress on a water-filled soil stems from the pressure exerted by the water column, which is measured as hydraulic head. Due to the elasticity of both the solid matrix and the water in the voids this leads to a variability of the amount of stored water (Fetter, 2001). For one, an increasing pressure induces a contraction of the solid matrix and thus increases the effective porosity. Additionally the water itself is compressed in this case, thereby allowing for more water to be stored. The specific storage S_s (m) accounts for this effect. It is defined by

$$\frac{\partial \rho \phi}{\partial t} = \rho g (\beta_p + \phi \beta_w) \quad (2.4)$$

with the density ρ (kg m^{-3}) of water, the standard gravity g (m s^{-2}), the compressibility of the bulk aquifer material β_p ($\text{m}^2 \text{N}^{-1}$) and the compressibility of water β_w ($\text{m}^2 \text{N}^{-1}$). Specific yield and specific storage represent two different material properties of an aquifer. they are summarised by the dimensionless storativity S (Fetter, 2001),

$$S = S_y + b S_s \quad (2.5)$$

where b denotes the water-filled thickness of the aquifer. Graphically, the storativity is the volume of water V_w absorbed or expelled from storage of a permeable unit per unit surface area A and unit change in head h (Fetter, 2001),

$$S = \frac{1}{A} \frac{\partial V_w}{\partial h} \quad (2.6)$$

For unconfined aquifers the contribution from the specific yield is much larger than the contribution from the specific storage to the storativity (Todd and Mays, 2005). For draining confined aquifers however, the specific yield equals zero as long as they remain water saturated (Fetter, 2001). Thus, the specific storage of a confined aquifer can be approximated by

$$S_s = \frac{S_y}{b} \quad (2.7)$$

2.2 The Groundwater Flow Equation

For water flowing in an aquifer conservation of mass can be assumed. Furthermore, the aquifer can be divided into a number of small control volumes $dV = dx dy dz$ with side lengths dx dy and dz in x -, y - and z -direction, respectively. On each of these control volumes a mass balance can be written, where the change in stored mass dM/dt in the volume over time equals the difference in rates of inflowing water mass \dot{M}_{in} , outflowing water mass \dot{M}_{out} and water mass added or withdrawn by sources or sinks \dot{M}_{ss} ,

$$\frac{dM}{dt} = \dot{M}_{in} - \dot{M}_{out} + \dot{M}_{ss} \quad (2.8)$$

The mass flow rates can also be written in terms of water density $\rho(\mathbf{x}, t)$ and fluxes $\mathbf{q} = (q_x, q_y, q_z)$ through the surfaces $(dx dy)$, $(dx dz)$ and $(dy dz)$ of the control volume. Assuming a constant density $\rho(\mathbf{x}, t) = \rho$ and letting the side lengths tend towards zero gives

$$\frac{dM}{dt} = \rho dx dy dz \left(\frac{\partial q_x}{\partial x} + \frac{\partial q_y}{\partial y} + \frac{\partial q_z}{\partial z} \right) \quad (2.9)$$

With Darcy's law the fluxes q_i can be estimated through the changes $\partial h / \partial x_i$ in hydraulic head h ,

$$q_i = \sum_{j=x,y,z} \left(K_{ij} \frac{\partial h}{\partial x_j} \right) \quad (2.10)$$

where K_{ij} denote the respective hydraulic conductivities. Without loss of generality the coordinate axes of the control volume can be chosen parallel to the major directions of the porous medium, so that the non-diagonal terms of the hydraulic conductivity tensor equal zero, $K_{ij} = 0 \forall i \neq j$. Therewith Equation (2.9) becomes

$$\frac{dM}{dt} = \rho dx dy dz \left(\frac{\partial}{\partial x} \left(K_{xx} \frac{\partial h}{\partial x} \right) + \frac{\partial}{\partial y} \left(K_{yy} \frac{\partial h}{\partial y} \right) + \frac{\partial}{\partial z} \left(K_{zz} \frac{\partial h}{\partial z} \right) \right) \quad (2.11)$$

The stored water mass M on the left hand side is generally given by the density of water $\rho(\mathbf{x}, t)$ and the water volume inside the control volume. This volume is given according to Equation (2.2) by the effective porosity ϕ_{eff} and the total volume of the control volume $dV = dx dy dz$,

$$M = \rho(\mathbf{x}, t) \phi_{eff} dV \quad (2.12)$$

Here dV is by definition constant over time. However both water density and effective porosity depend on the stresses exerted on the control volume and are therewith functions of space and time. Thus follows

$$\frac{dM}{dt} = dV \frac{\partial(\rho(\mathbf{x}, t) \phi_{eff})}{\partial t} \quad (2.13)$$

Through application of the chain rule the right side can be expressed through the specific storage S_s and the change in hydraulic conductivity. As for Equation (2.9) constant density ρ is assumed. This ultimately leads to the groundwater flow equation:

$$S_s \frac{\partial h}{\partial t} = \frac{\partial}{\partial x} \left(K_{xx} \frac{\partial h}{\partial x} \right) + \frac{\partial}{\partial y} \left(K_{yy} \frac{\partial h}{\partial y} \right) + \frac{\partial}{\partial z} \left(K_{zz} \frac{\partial h}{\partial z} \right) + \dot{M}_{ss} \quad (2.14)$$

Chapter 3

Study Region: The Chtouka-Massa Plain

3.1 Localisation

- In this study, a model for the Chtouka aquifer is examined. The Chtouka aquifer underlies the agriculturally important Chtouka-Massa plain.
- It is located bordering the atlantic ocean and is part of the over 27,000 km² extending Souss-Massa River Basin in south-western Morocco (Figure 3.1).
- The Souss-Massa River Basin is comprised of the watersheds of the rivers Souss in the north and north-east and Massa in the south.
- The former originates in the mountains of the High Atlas to the north, the Siroua Massif to the east and the Anti Atlas to the south-east, and the latter in the Anti Atlas to the east and south-east.
- These mountains and their foothills accordingly constitute the boundaries of the basin to the north, east and south, while the Atlantic Ocean forms its boundary to the west.
- Below 700 m.a.s.l. and down to 0 m.a.s.l. lies the triangular-shaped, extensively agriculturally developed Souss-plain embedded (Choukr-Allah et al., 2017).
- This plain has an area of 5,700 km², of which the Chtouka-Massa area incorporates 1,300 km².
- This latter area in turn extends over approximately ranges from 0 m.a.s.l. on the western Atlantic coast up to 440 m.a.s.l. in the south-eastern mountainous area. Sloping from east to west, 80 % of its surface are between 50 and 175 m.a.s.l..

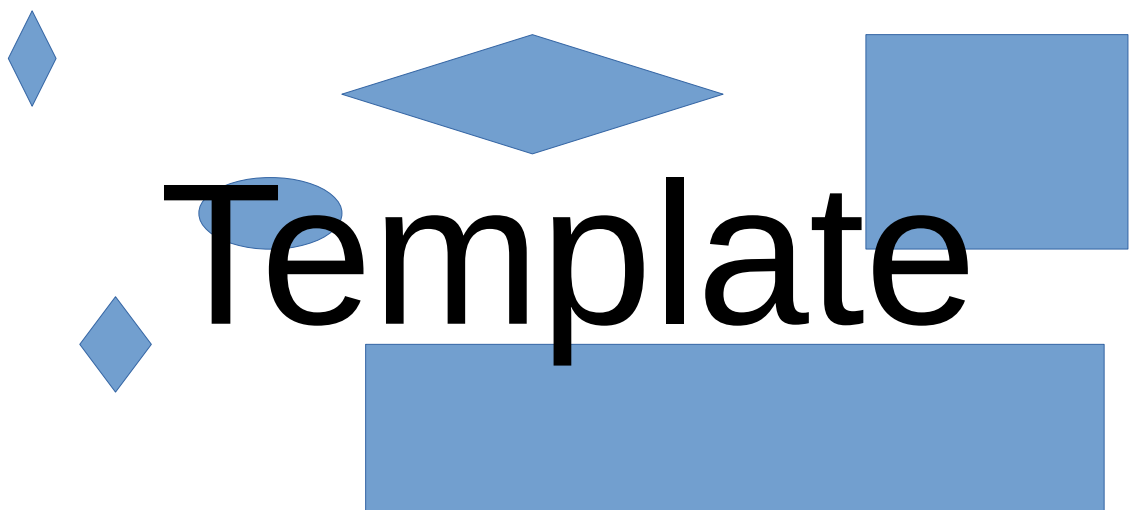


Figure 3.1: Map of the Souss-Massa basin, which contains the Chtouka aquifer. This representation was derived from digital elevation model data of NASA JPL, 2013 and follows in topographical colouring Hssaisoune et al., 2017. ...

3.2 (Hydro)Geology

- The Souss-Massa plain has been formed by the homonymous rivers and their tributaries and is covered by their alluvial deposits (Hssaisoune et al., 2017).
- Therefore the Chtouka aquifer can be characterised by four different major Plio-Quaternary geological formations that can be identified following Malki et al., 2017, who derived the division from several other studies:
 - (i) in the southern and eastern parts of the plain marls and limestones basing directly on Acadian age schist,
 - (ii) conglomeratic deposits in the beds of the Massa,
 - (iii) sands and silts as alluvial deposits from the recent Quaternary and
 - (iv) lacustrine limestones with large spatial extension.
- For further information, see Choubert, 1964, Hssaisoune et al., 2017, Horn, 2021 and Krimissa et al., 2004.

3.3 Climate

- Generally, climatic conditions in the Souss-Massa River Basin are semi-arid (Choukr-Allah et al., 2017).
- However, some spatial variability can be observed. In the Souss-Massa plain annual rainfall averages at around 250 mm a^{-1} , while in the mountains average annual rainfalls are at around 600 mm a^{-1} . This leads to the surface water supply in the plain being higher than its local climate may suggest (Hssaisoune et al., 2017).
- Annual rainfalls over the last decades in Biougra, a city in the Chtouka-Massa plain and a climate chart for the region are shown in Figure 3.2.
- According to this chart and following the modified Köppen system as described in Critchfield, 1983, also the Chtouka-Massa area in specific has a semiarid climate (Choukr-Allah et al., 2017).
- In the Chtouka-Massa area, the long-term average precipitation is about 187 mm a^{-1} .
- Over the years, rainfalls show a high variability between years with over 600 mm a^{-1} (three times the long-term average) in humid years and less than 50 mm a^{-1} (a quarter of the long-term average) in dry years.
- Potential evapotranspiration on the other hand lies at approximately 2000 mm a^{-1} in the the Souss Massa River Basin (Choukr-Allah et al., 2017) and therewith significantly exceeding water supplies through rainfall, as typical for arid and semi-arid climates.
- It may be noted that as basis for yearly measurements the local hydrological year in the period from 1st of September of one year to 31st of August of the following one is used. Following this convention, in this work this specific hydrological year is always implied, whenever a "year" is referenced. For ease of reading however, instead of the full label (e.g. "2021/22") only the first calendar year will be shown in labels ("2021").

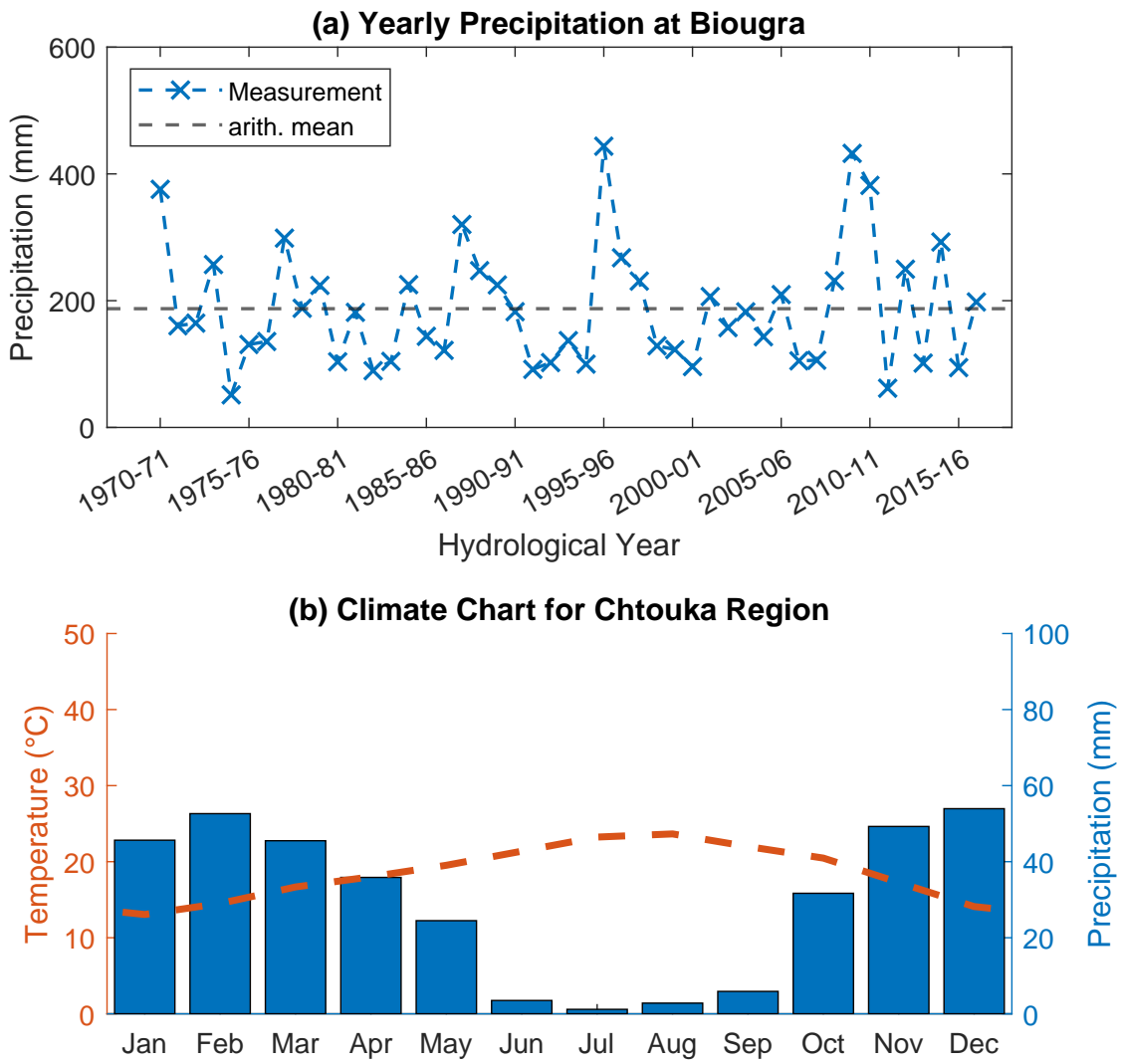


Figure 3.2: Climatic conditions in the Chtouka-Massa plain. (a): Annual precipitations at the city of Biougra in the period 1970 to 2016. Measured are the respective hydrological years, from 1st of September of the denoted year to 31st of August of the following year. The underlying dataset was provided by the ABHSMD. (b): Long-term average temperatures and precipitation during a year. The climate chart bases on data for the years 1950-2017 and is derived from the gridded monthly time series datasets Matsuura and Willmott, 2018a and Matsuura and Willmott, 2018b.

3.4 Structure of the Region

- On federal level, agriculture has a growing contribution to the Moroccan GDP, from 7 % in 1998-2008 to 17 % in 2008-2018 and thus plays a key role in Morocco's economical development (MAPMDREF, 2021).
- In this sector the Souss-Massa plain is economically the second most important region in Morocco (Choukr-Allah et al., 2017).
- The economy of the region is primarily founded on the high-value agricultural production, tourism and fishery.
- Covering more than one fifth of this area the Chtouka-Massa plain accounts for a significant portion of the agricultural production of the region (Choukr-Allah et al., 2017).
- Population
 - On administrative level, the Chtouka-Massa area is part of the Chtouka-Ait Baha province, which reaches to the east past the plain and further into the Anti Atlas mountains.
 - In this province a total population of 371,102 people was counted in 2014, of which 113,531 people lived in one of the four urban centres (Ait Baha, Biougra, Belfaa, Massa) and the rest in the 18 rural communes (DRSM, 2020).
 - In the period between 2004 and 2014 the population of the province had an average annual growth rate of 2.24 % (DRSM, 2020).
 - As shown by these numbers, the Chtouka-Massa plain is a primarily rurally characterised area.
- Agriculture
 - With a year-round growing season, the Souss Massa River Basin accounts besides other products for more than half the production of Moroccan citrus and vegetables (Hssaisoune et al., 2017).
 - In the Chtouka-Massa plain, majorily tomatoes and peppers are cultivated in greenhouses (DRSM, 2020) and furthermore other vegetables and fruits, cereals, fodders, ornamental crops and deciduous trees (ORMVASM, 2015).
 - Surveys from 2015 identified a total number of 2724 farms covering an area of approximately 24,800 ha and which employ more than 40,000 persons (ABHSMD, 2015).
 - The majority of these farms are located around Ait Amira, Belfaa, Biougra, Sidi Bibi and Massa (confer Figure 3.3).

- As the whole region of the Souss Massa River Basin (Choukr-Allah et al., 2017), irrigated areas in the Chtouka-Massa plain show an continuous expansion in the past decades.
- irrigation techniques
 - In the area, three different irrigation practices are being used. The traditional flooding method, as well as sprinkler and drip irrigation.
 - These different irrigation techniques exhibit different water usage efficiencies, with flooding being the least and drip irrigation being the most efficient.
 - Simultaneously, these methods require a different technological development and therewith investment of farms, which is why their application highly depends on the economical organisation and situation of farms (Choukr-Allah et al., 2017).
 - Thus, the implementation of the different techniques varies both spatially and temporally over the agricultural area.
 - Due to the problem of overexploitation of water resources (see Section 3.5), following the agricultural strategy plan "Plan Maroc Vert" which was adopted in 2008 and its National Irrigation Water Saving Program, efforts have been made to significantly increase the portion of water efficient drip irrigation in the past 15 years (MAPMDREF, 2021).
 - For instance, in the northern and north-western public perimeter where structured agri-business farms predominate, an extensive conversion to drip irrigation took place in recent years (ABHSMD, 2015).
 - At the same time, in the centrally located public perimeter sprinkler irrigation is still the predominant method.
 - Furthermore, in these two perimeters cultivation widely takes place in greenhouses.
 - At the traditionally farmed Tassila perimeter in the south, along the Massa River, water-intensive flooding is still the major technique.
 - The extents of the different perimeters varied over the decades. Their respective estimated boundaries for the period 2010-2019 are shown in Figure 3.3.

3.5 Hydrology

(maybe rather as the subsequent section to Climatology?)

- **Natural Water Resources and Hydrographic Network**

- **Souss Massa River Basin**

- In the Souss Massa River Basin, in average $1,093 \text{ Mm}^3$ are available (ABHSMD, 2005), consisting of 36% surface water and 64% ground water (Choukr-Allah et al., 2017).
- Surface water is mainly provided by the two homonymous rivers.
- Depending on the current rainfall, surface water potential shows a large variability from year to year (Choukr-Allah et al., 2017, ABHSMD, 2022).
- To regulate the flows of both rivers and ensure a regular supply of water, in the Souss Massa River Basin a total of eight dams have been built in the period from 1972 to 2004 (Choukr-Allah et al., 2017).
- These dams have a total potential capacity of $730,404 \text{ Mm}^3$ (as of 07.09.2022 holding $83,552 \text{ Mm}^3$ (ABHSM, 2022)). Of these the Youssef Ben Tachfine (YBT) dam, put into service 1972, bordering the Chtouka-Massa plain in the south is the largest with a potential capacity of $298,200 \text{ Mm}^3$ (as of 07.09.2022 holding 43.222 Mm^3) (ABHSM, 2022).
-
- The Souss River originates to the north in the High Atlas mountains where its tributaries form a dense drainage network and to the south in the Anti Atlas where the tributary network is lighter (Hssaisoune et al., 2017).
- After confluencing from its different tributaries, the river flows into the from west to east over 182 km extending plain, from which it ultimately discharges to the west into the Atlantic Ocean at the cities of Ait Melloul and Agadir.
- Its flow is strongly seasonal, and during rainy years high floods can occur between October and February (Hssaisoune et al., 2017).
- The Massa River, which forms the southern boundary of the Chtouka-Massa plain, originates in the Anti Atlas Mountains, from where it flows in western to north-western direction towards the Atlantic Ocean.
- At the southern-most corner of the aquifer it supplies the biggest reservoir of the Souss Massa River Basin, the one retained by the Youssef Ben Tachfine (YBT) dam (Figure 3.4), which regulates the Massa's flow on the following 36 km to its estuary at the Atlantic Ocean.
- Downstream of the dam, the river first flows in a small channel of 5 to 10 m width with a higher absolute topographic gradient. Subsequently when reaching around the village of Iftenar the flatter part towards the coast, it flows in a wider, meandering channel (Horn, 2021).

- The Massa exhibits a high variability following annual and interannual climatic irregularities characterised by brief floodings interrupted by long periods of dryness (Hssaisoune et al., 2017), for which it is also called Oued Massa ("Wadi Massa").
- From the YBT dam, a channel originates that leads into the public irrigation perimeter (Figure 3.3).
- Overall, the principal water resource of the Souss Massa River Basin is provided by the groundwater of its aquifers and the eight dams (Hssaisoune et al., 2017).
- The groundwater reservoir is situated solely below the Souss-Massa plain and therewith only up to 700 m.a.s.l., as the higher parts are mountainous.

- **Chtouka Aquifer**

- Although water supply in the Souss Massa River Basin consist of both surface water in the homonymous two rivers and groundwater, in the Chtouka-Massa area groundwater constitutes the major water source. Surface water is at most times only lead by the Oued Massa along its southern boundary and the channel from the YBT dam.
- On occasion, additionally some oueds lead water from the Anti Atlas into the Chtouka-Massa plain. These however only represent intermittent water sources.

- **Water Demands**

- **Souss Massa River Basin**

- In the Souss Massa River Basin, water demand is composed of 12.5 % drinking water and water for industrial use, and 86 % for agricultural purposes (Choukr-Allah et al., 2017).
- In water demand a seasonality can be observed, as irrigation and tourism are in summer more extensive, while at the same time natural water supply is minimal (Choukr-Allah et al., 2017).

- **Chtouka Aquifer**

- In the hydrological year 2018 51,018 Mm³ for irrigation and 8,208 Mm³ for drinking purposes was withdrawn from the YBT Dam (ABHSMD, 2022).

- **Development of Water Resources**

- **Souss Massa River Basin**

- In the Souss Massa River Basin water exploitation increased significantly in the last decades due to increased irrigated agriculture, tourism and industrial development (Choukr-Allah et al., 2017, Hssaisoune et al., 2017).
- Therefore groundwater levels decreased over the past four decades within a range of 0.5 – 2.5 m a⁻¹ due to overpumping (Choukr-Allah et al., 2017) (Hssaisoune et al., 2017).

- This led to deterioration of groundwater due to saltwater intrusion in coastal areas and deep well drilling over the past decade (Choukr-Allah et al., 2017).
- **Chtouka Aquifer**
- For the Chtouka aquifer, the water imbalance between recharge and withdrawal of groundwater leads to an annual destocking of $58 \text{ Mm}^3 \text{a}^{-1}$ (ABHSMD, 2014).
- Furthermore the quality of the water resources degraded in the course of the last decades due to pollution mainly stemming from domestic, industrial and agricultural wastewaters and fertilisers. Especially nitrate concentrations exceed in 36 % of wells in the Chtouka-Massa plain the regulatory threshold of 50 mg l^{-1} for drinking water (Choukr-Allah et al., 2017).
- In the next decades water demand is expected to further increase in the whole region due to population growth, increase in per capita consumption and extension of irrigated agriculture (Choukr-Allah et al., 2017).
- Simultaneously a decline in water availability is expected due to overpumping of groundwater and lower recharge through rainfalls, which in turn is caused by proceeding urbanisation and climate change (Choukr-Allah et al., 2017 Hssaisoune et al., 2017).
- To tackle these issues, in 2008 the "Plan directeur d'aménagement intégré des ressources en eau (PDAIRE)" was created. Besides a revised and intensified management of available water resources and the efficiency enhancement of water consumption, it aims at the exploitation of unconventional water resources such as wastewater reuse and the desalination of seawater (Choukr-Allah et al., 2017).

3.6 Unused Additional Information

- Over all, due to recent population growth, urbanisation, tourism, industrialisation, globalisation and climate variability as well as change - which in turn induces a decrease of precipitation and an increase of the frequency of droughts - increasing water scarcity affects the region (Choukr-Allah et al., 2017).
- In the Souss-Massa region, a population of 2.56 million people was counted in 2014 with an annual growth rate of 1.4 %. Of these, 55 % live in rural areas.
- "The Souss-Massa plain is a narrow fainting zone with recent sedimentary deposits, embedded between the High Atlas in the north and the Anti Atlas in the south." (Hssaisoune et al., 2017)
- more than half of the production of exported citrus and 85 % of exported vegetables of Morocco (which vegetables?)
- main crops: cereals, citrus, banana, tomato, other vegetables

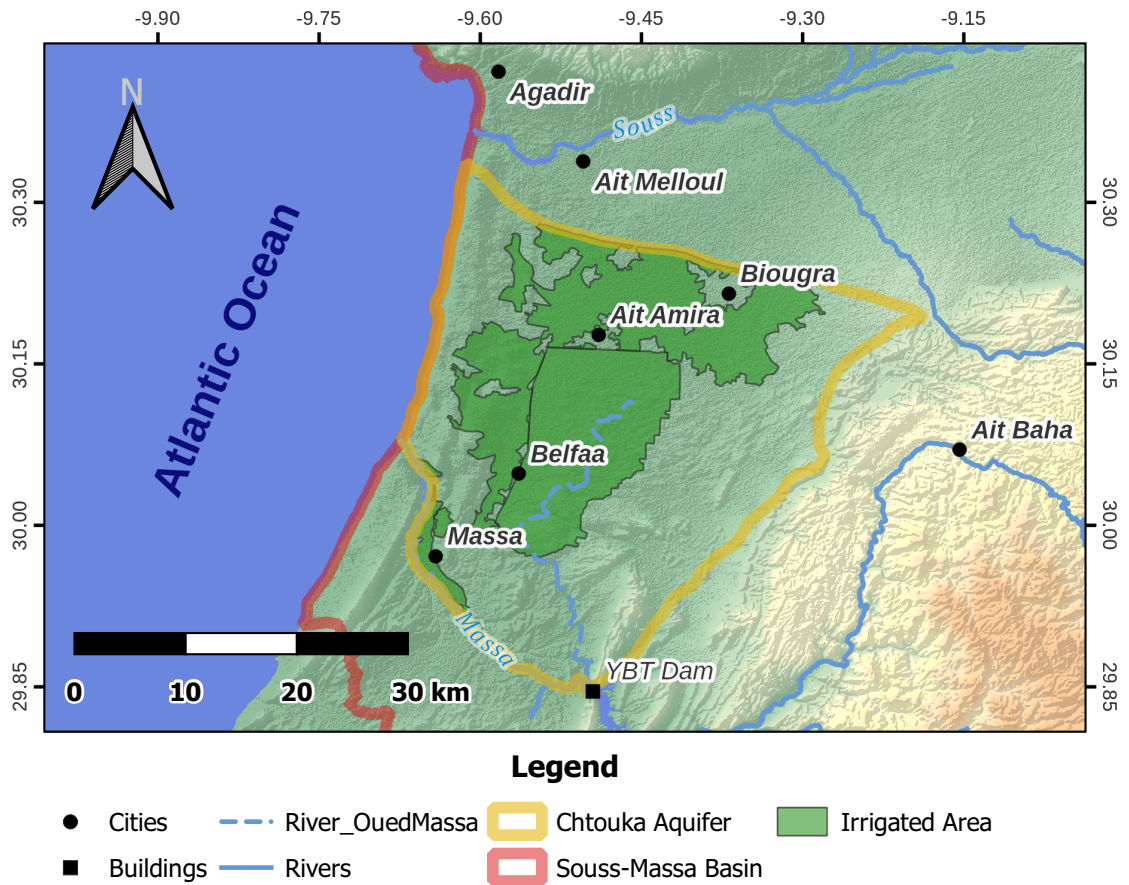


Figure 3.3: A Map showing the Chtouka-Massa plain in the Souss Massa River Basin. The map is derived from the digital elevation model data of NASA JPL, 2013 accessed through USGS, 2018. [To be revised: name of channel, representation of water bodies: main oueds and intermittent oueds, different colouring of agri-perimeters, "cities" renamed to "municipalities", adding of ≥ 2 more cities: Sidi Bibi and one on eastern boundary; north arrow same colouring as scale;...?]

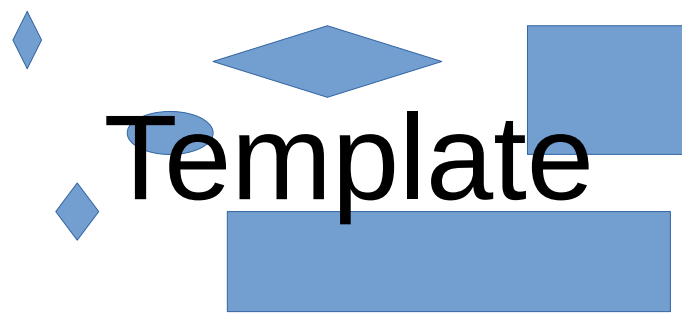


Figure 3.4: Photograph of the YBT dam. [could be deleted, as not really necessary; would only add a nice picture to the text]

Chapter 4

Conceptual Model/Model Geometry

Introduction:

- present the balance of the aquifer from which the conceptual model derives its different layers
- these different layers will be presented in the following sections
- note that Model Delineation and Geological Model do not follow from this; the prior moreover determines the water balance and the latter has no direct influence on the schematic balance; however their description is still part of the conceptual model
- measured as/target quantities as follow from the gwflow equation (ref)

4.1 (Horizontal) Delineation of the Model

- The Chtouka Aquifer is located underneath the Chtouka-Massa plain.
- For delineation in the xy -plane, a set of four boundaries, each characterised by a particular type of boundary condition has been identified by Horn, 2021.
- These different boundaries approximately follow the orientation of the model outline in space and are therefore named as *northern*, *eastern*, *southern* and *western boundary*. The four boundaries are shown in Figure ??.

4.1.1 Northern Boundary

- The northern boundary is defined as a Neumann no-flow boundary. It follows a by Horn, 2021 estimated streamline derived from a contour map of the groundwater table in 1968 by Bernet and El Hebil, 1977 which therewith presents a groundwater divide.

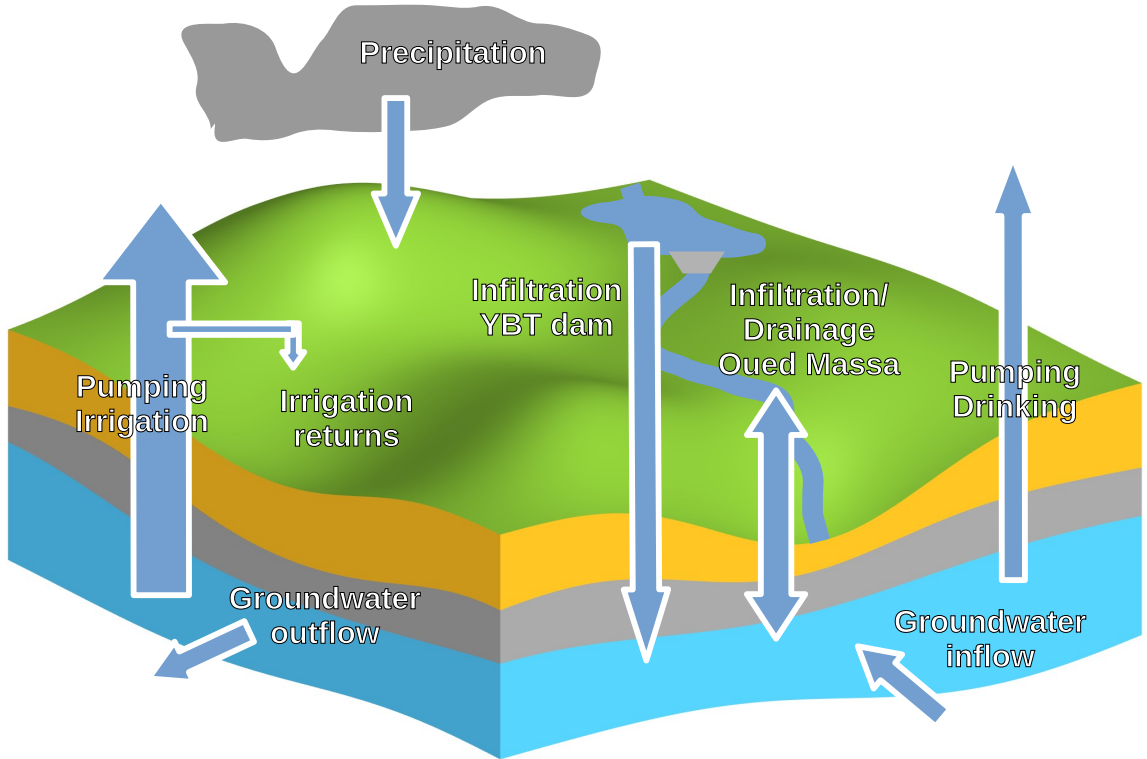


Figure 4.1: The water balance of the system. [Arrows and labels will be revised to look better, as well as the cloud for precipitation]

- The boundary runs from the north-eastern corner of the model over 45.3 km in north-western direction to the coast of the Atlantic Ocean. Even though streamlines change depending on groundwater levels and their spatial and temporal variation, due to lack of data this boundary is assumed as constant over the modelling period.

4.1.2 Eastern Boundary

- For this study, at the eastern boundary an adjusted version of the specified head boundary (Dirichlet) by Horn, 2021 is used with estimated transient heads.
- The course of the boundary is redefined along the transition zone between the foothills of Anti Atlas mountains and the Chtouka-Massa plain.
- The head stages along the boundary naturally vary in both space and time.
- For their estimation the following data is available:
 - (i) bottom elevations of the aquifer along the boundary,

- (ii) surface elevations from the DEM and
- (iii) piezometric measurements at different times and positions within a perimeter along the boundary of 1.5 km radius.
- Most of these latter observations stem from initial measurements done when bringing new groundwater wells into service, and therewith represent single point-in-time measurements.
- This data encompasses three measurements before the modelling period starting in 1968, of which one dates back to 1958 and two to 1967.
- For the period from 1968 to 2003 a total of 14 more such measurements at different locations are available.
- Furthermore, at one location 8 km from the north-eastern corner of the model region a time series exists, covering the hydrological years 1968 to 1995 with temporal resolutions ranging between monthly and once every two years.
- Another time series, with a coverage of 10 measurements over 1.5 years much shorter time series is due to its only little variation of less than 1 m considered as single point-in-time measure.
- With this data the initial head in 1968 is estimated at 29 locations on the boundary basing on three characteristics:
 - (i) measurements from 1968,
 - (ii) extrapolated measurements from earlier and later hydrological years, such that the amplitude of head variations over the years is of the same order as the one observed in the time series and
 - (iii) following the natural topography of the aquifer.
- In between these 29 locations, heads are linearly interpolated along the course of the boundary.
- The result is shown in Figure 4.3.
- From this initial boundary condition, using the available observations the temporal evolution of heads at the boundary is estimated for the hydrological years 1985, 1995 and 2005. In between these years, a linear evolution of the heads is considered.
- For the period after 2005 no further information is available and thus the heads are then assumed as constant.

4.1.3 Southern Boundary

- The southern boundary is defined by the Oued Massa.
- Due to both the temporal and spatial variability of the flow regimes along the river, changing influent and effluent conditions of the aquifer occur along this boundary. To account for this, Horn, 2021 implemented this boundary as River type boundary condition into GMS.
- Hence it is characterised through three parameters: the bottom elevation, the head stage and the riverbed conductance.
- Thereof, the bottom elevation is defined by the used DEM.
- The head stages are estimated by an assumed linear relation between the discharge rate measured at the YBT dam and the assumed average water level in the river. these discharge rates can be extracted from data of daily water balances in the YBT reservoir. As these measurements were taken only from 1975 onwards, two different time periods need to be distinguished defined by the available data: The period before 1975 and the time after. For the prior time period from 1968 to 1975 head stages are estimated from annual rainfalls (see Horn, 2021 for further details).
- The conductance C (m s^{-1}) is estimated as conductance per unit length by

$$C = \frac{k}{t}w \quad (4.15)$$

- where k (m s^{-1}) is the hydraulic conductivity of the riverbed, t (m) the riverbed thickness and w (m) the width of the river (Aquaveo, 2019).
- For the hydraulic conductivity values lower than those of the underlying lithological unit are assumed, as sedimentation may lead to clogging processes.
- As described in Section 3.5, the Oued Massa can be divided into two different parts: an upstream part ranging from the YBT dam to the village of Ifentar, and a downstream part from Ifentar to the Atlantic Ocean. Therefore, on these two sections different assumptions define the applied parameters of river width and riverbed thickness. Higher flow velocities in the narrow upstream part lead to higher erosion and lower sedimentation in the river bed and thus a thinner riverbed is assumed. In the wider downstream part on the other hand less erosion and higher sedimentation occurs, leading to a thicker riverbed.

4.1.4 Western Boundary

- The western boundary is defined as a Dirichlet constant head boundary. Its shape is defined by the coast of the Chtouka-Massa plain along the Atlantic Ocean. Therefore it runs over 31.8 km in south-south-western direction from the north-western corner of the model. Head stages at this boundary are assumed as constantly at the sea level of the DEM from NASA JPL, 2013 over the whole modelling period.

4.2 Geological Model

In a preceding work, Horn, 2021 derived a geological model of the Chtouka Aquifer (Figure 4.4) on the basis of lithological drilling data from 100 boreholes, geophysical measurements and data from geological maps of the region. This model is used in this study and shown in Figure 4.4. In the following, its main characteristics will be summarised. For more detailed information refer to the cited study.

Over the modelling area, a distinction into a total of five different lithological units, each assumed as homogeneous over its spatial extent, was identified. These units are:

- calcareous marl,
- sand,
- schist,
- gravel and
- silty sand.

Of these, calcareous marl, sand and schist form the group of main units with large spatial extents.

- Schist is considered to be the oldest stratigraphical unit. It outcrops at the eastern part of the aquifer and is covered by sediments towards the west.
- Above the schist lies in most regions a layer of calcareous marl with a mean thickness of 100 m. Although showing in reality local variations between more sandy and more clayey areas, it is over-all assumed as one lithological unit.
- Apart from an area in the south where this lithological unit outcrops, calcareous marl is covered by one of the three remaining strata.
- Predominantly the overlying layer is sand, which also forms the top of the aquifer in most areas. While reaching its estimated maximum thickness of 150 m along the coast, the layer thins towards the eastern part.

- The north east of the model is characterised by alluvial fans of in both horizontal and vertical direction varying compositions of clay, sand and gravel. This area is modeled by the two lithological units silty sand and gravel.
- Each one of the five geological units is defined by its specific material properties, which are the hydraulic conductivities K_h in horizontal and K_v in vertical direction (both (m s^{-1})) as well as the corresponding horizontal and vertical anisotropies (–), the porosity ϕ (–), the specific yield S_y (–) and specific storage S_s (m^{-1}) and the longitudinal dispersivity (–).

- **vertical delineation**

- **top**

- The top of the aquifer is determined as the area's surface and is defined by the digital elevation model of NASA JPL, 2013, which has a $30 \text{ m} \times 30 \text{ m}$ resolution. It was accessed via USGS, 2018.

- **bottom**

- The bottom boundary of the aquifer is defined by Horn, 2021 depending on the local stratification of the lithological units.
- As basis, unweathered schist is generally assumed to be a towards the bottom confining (aquitard/bedrock?). In turn, schist may become a water bearing stratum due to weathering. Following McFadden et al., 2005 this weathering is considered to reach at most 50 m into the unit. This maximum depth may occur only in regions where the schist crops out, as this is the case in the eastern parts of the model area. Where the schist is overlain by other strata, the weathered depth should accordingly be reduced (Note: This however is not directly stated in Horn, 2021, but follows from the fact that in the model schist also appears in regions where it is not the top layer). This leads to a minimum depth of the aquifer of 50 m in relation to the local surface elevation in all regions.
- In the central area, thicknesses of the aquifer are estimated by the depths of the locally deepest drilled wells.
- In the northern part of the Chtouka aquifer, data from measuring campaigns of vertical electrical soundings in the period 1947 to 2008 in the Souss Massa River Basin are used to define the bottom of the aquifer.
- For the coastal areas, transient electromagnetics measurements (Schreiber et al., 2021) (correct reference?) from a campaign within the framework of the CREM [so far missing: explanation of CREM project, maybe in introduction?] project are used.

4.3 Recharge from Precipitation

- The here used data for recharge from precipitation was compiled by Horn, 2021 and will be briefly described in the following. For more information, refer to the cited study.
- Precipitation
 - For estimations of the local precipitation datasets from meteorological stations in Agadir, Ait Melloul, Ait Amira, Biougra and at the YBT dam were available.
 - Basing on this data three zones are identified, which account for the spatial variations of precipitations due to regional differences in altitude and climate. These zones are shown in Figure ??.
 - The northern-most zone has the highest average annual precipitation of 220 mm a^{-1}
 - The central zone, which incorporates the largest area of the model region, and the southern-most zone are characterised by a significantly lower annual precipitation of 170 mm a^{-1} respectively 160 mm a^{-1} .
- Infiltration
 - The infiltration rates of the precipitation are estimated basing on the top-most lithological unit and expected evaporation from the ground.
 - Therefrom infiltration rates of 6 % of the precipitation follow for the northern and central area and 5 % for the southern area.
 - The derived annual time series of recharge from precipitation are shown for the three areas in Figure 4.5.

4.4 Groundwater Wells

- Groundwater extraction through wells has been examined in various studies by the ABHSM(D?).
- Thus, data is available from different databases. This data has been previously analysed by the project team and processed to fit the modelling needs. In the following, the main features are summarised. For detailed information refer to the technical notes in Appendices A and B in Horn, 2021.
- Each well is characterised by a name, its location in the xy -plane and its top elevation, the depth to top of the screen and the screen length as well as by a time series of estimated or measured flow rates.

- All wells can be distinguished into two classes. The first class encompasses manually dug wells, the second drilled and reconnaissance wells.
- This classification has been used to interpolate missing data concerning the vertical screen locations and screen lengths of some wells.
- Furthermore, the wells can be additionally classified through the utilisation of the extracted water, which is either for drinking and domestic purposes or for irrigation.
- Basing on the membership to one of these classes, pumping rates have been estimated for wells with missing data.

4.4.1 Drinking Wells

- A total of 650 wells are considered as drinking wells in the study area. These are depicted in Figure 4.6(a).
- Data on extracted water volumes are available for the time periods 1969-2001 from one single source and 2001-2020 from several sources, varying in their respective basic populations.
- Basing on these datasets pumping volumes and therewith pumping rates are estimated for the whole period from 1969 to 2020.
- Information on commissioning of new wells is only available for the time period until 2003, in which a rapid increase in the number of wells occurred.
- For the time after 2003, the further commissioning of wells is assumed as being coupled to the population growth and is assigned a yearly growth rate of 0.7%, thus slowly increasing the extracted water volume.

4.4.2 Irrigation Wells

- Data regarding the irrigation wells is available from several studies from the years 2003 and 2015.
- In the study from 2003, a total of 2448 wells are recorded and in 2015 a number of 3050 wells. Due to significant differences in either location (the vast majority) or in well characteristics (21 wells in total) both sets of wells are considered as disjunct. Therewith a total of 5498 irrigation wells is considered in this study (Figure 4.6(b)).
- Data from the studies base on personal records or memorizations from farmers and estimates for each well or each farm made during the surveys.

4.5 Irrigation Returns

- As described in Section 3.4, the Chtouka plain is extensively used for agricultural activities.
- As stated introductory to this section, a certain portion of the applied water re-infiltrates into the aquifer and leads to groundwater recharge.
- To account for this recharge, both the spatial extents and the infiltration rates of the applied water are estimated as described in this section.
- The agriculturally occupied area can be divided into three differently administered perimeters: Firstly the private perimeter in the north around the municipalities of Biougra and Ait Amira and southwards along the coast, secondly the public perimeter in the central part of the plain and thirdly the Tassila perimeter in the south along the Oued Massa, around the municipality of Massa.
- An analysis of satellite pictures from different years shows that the boundaries of the public and the Tassila perimeters have been approximately constant for the whole modelling period.
- The private perimeter however exhibits a significant change over time.
- To account for this evolution, the perimeter's extents are estimated for six consecutive periods (1968-1973, 1974-1979, 1980-1989, 1990-1999, 2000-2009 and 2010-2020).
- Within the three perimeters the three different irrigation techniques flooding, sprinkler and drip irrigation are used. Inside each of the three perimeters, a homogeneous distribution of the applied techniques is assumed. Over time however, the frequency ratios of the different methods vary as previous studies show (Resing, 2003, ANZAR, 2016). Basing on these studies the temporal evolution of the frequency ratios is estimated for each of the three perimeters.
- infiltration rates are finally calculated depending on these distributions ... using equation ... in which the infiltration coefficient is defined by equation ...

4.6 Observations

- Piezometers available scattered over the study area
- in total 27 piezometers
- covering different time series

- at 3-4 locations: pairs of two piezometers, covering succeeding time series; reason: drawdown became locally so large that well screens fell dry; thus newer wells drilled deeper; from these wells for each pair a combined, longer time series; thus observations available at 23(24) different locations (which piezometer pair not used+why?)
- available data: head measurements
- normally, head data measured as depth to water level from top of piezometer
- the height of the top end of the piezometer in m.a.s.l. has been determined during their construction through differing methods
- these methods have different accuracies, so piezometers are here accordingly divided into two major groups:
- the first group encompasses piezometers for which the height (z -location) of the piezometer was determined by levelling measurements; due to the high accuracy of this method, an uncertainty of 1 m.a.s.l. is assumed for measured heads
- the second group encompasses piezometers for which the height (z -location) of the piezometer was determined by manual reading of a printed topographical map; this method is sensible to three kinds of errors: (i) errors of localisation on the xy -plane of the piezometer due to the used GPS-devices, (ii) errors of manual placement on the used topographical maps, (iii) reading errors of the heights on the topographical maps, especially when the contour lines are far from each other; therefore, measurements from these piezometers are assigned an uncertainty of 10 m.a.s.l.
- in one case (name?) an uncertainty of 5 m.a.s.l. is assigned (why?)

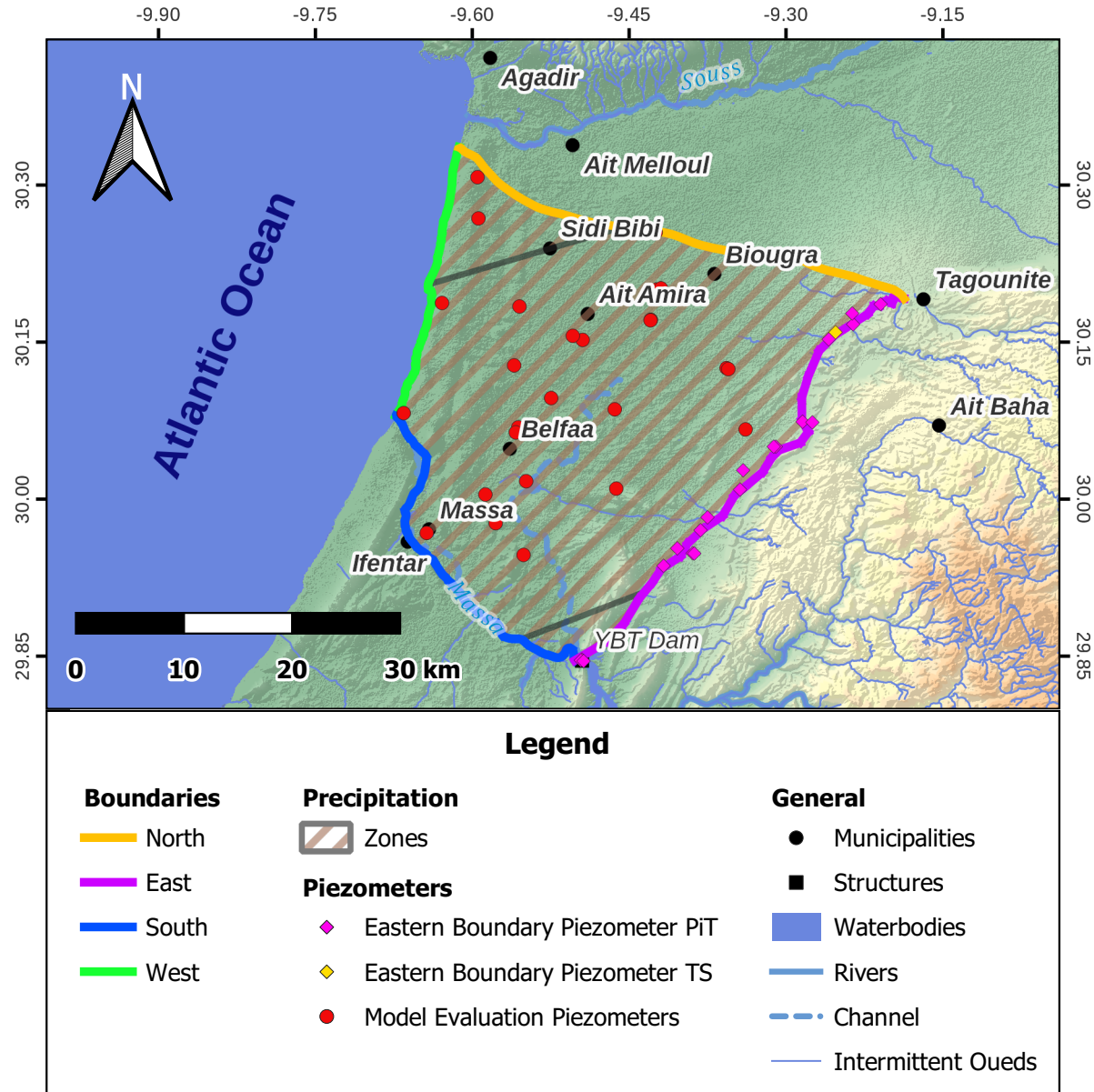


Figure 4.2: The delineated modelling area of the Chtouka aquifer. Shown are the four differently characterised boundaries (Section 4.1), the three different precipitation zones (Section ??) and the piezometers that are used for definition of the eastern boundary with differentiation between piezometers providing single point-in-time (PiT) and time series (TS) measurements (Section 4.1), as well as the piezometers for the model evaluation (Section 4.6). [adjust: background of prec-zones; instead: black line: boundaries of precipitation zones.]

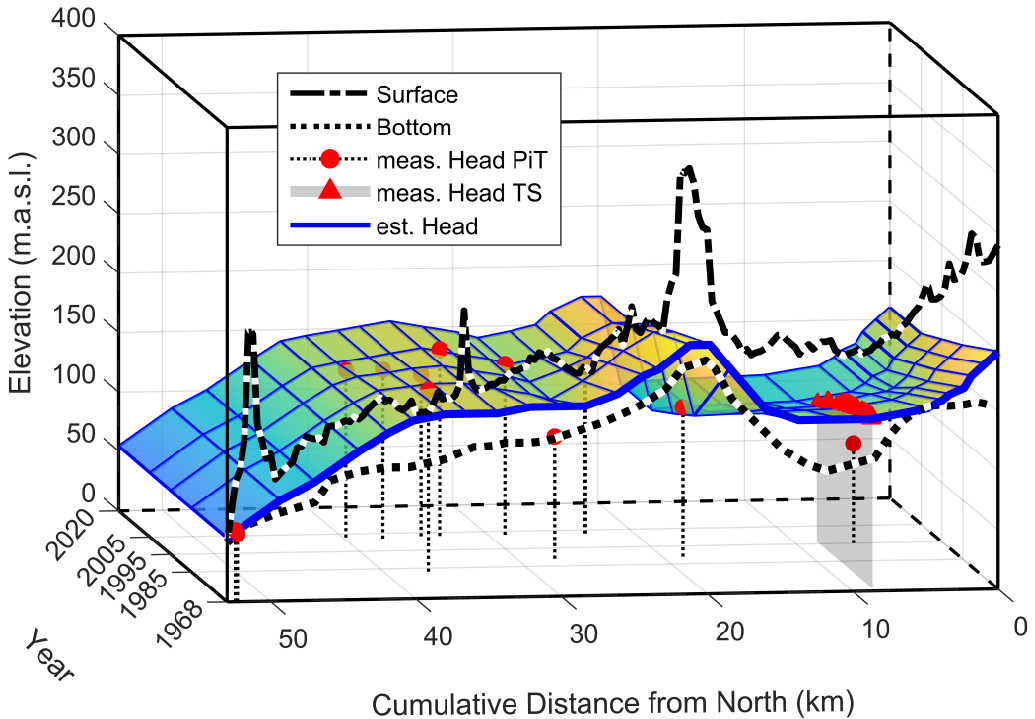


Figure 4.3: The adjusted Dirichlet boundary condition for the eastern boundary. The for 1968 estimated initial head (thick blue line) along with the bottom- (thick black dotted) and surface- (thick black dashed) elevations are shown at the starting year 1968. Measured heads are shown in red as circles for single point-in-time (PiT) measurements and as triangles for time series (TS) measurements. The grid (blue) spanning the temporal evolution of heads shows the linear interpolation in between the 29 locations and the five specified years. For better perceptability the surface marking the head stages in between these points is coloured according to head values.

Template

Figure 4.4: [Representation will be similar to the one from Horn, 2021, Fig. 5.1] The already discretised geological model of the Chtouka Aquifer, as defined by Horn, 2021. (a) presents a 3D view, with the black line denoting the crosssection shown in (b). It uses the chosen horizontal grid resolution of $500\text{ m} \times 500\text{ m}$ and 10 equally spaced layers in z -direction (see Section 5.1.4). The xy -plane is oriented along the four cardinal directions with the positive x -direction pointing to the north. For presentation purposes, a z -magnification with a factor of 10 is applied.

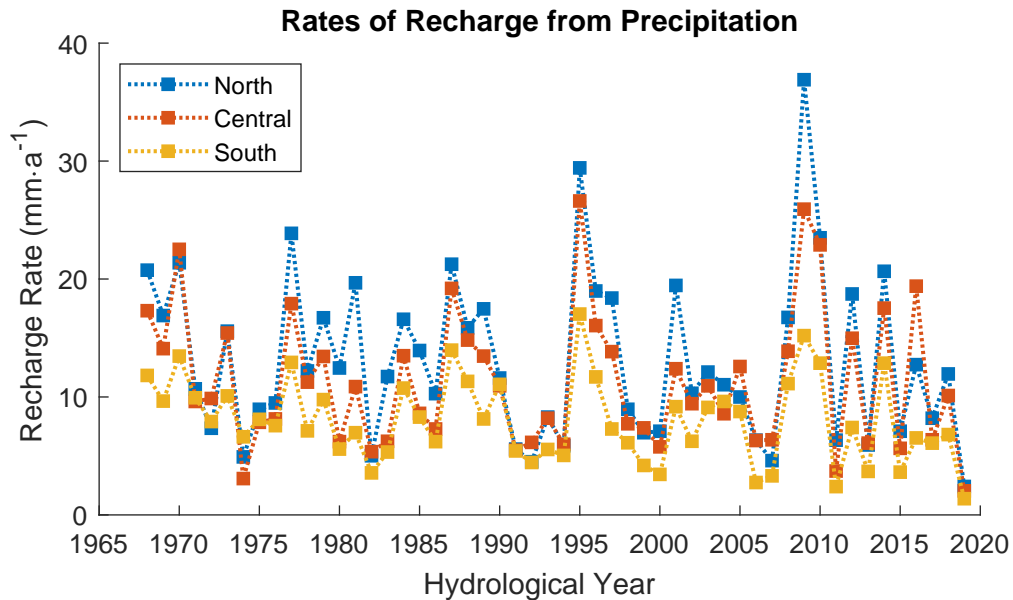


Figure 4.5: Time series of annual groundwater recharge in the three different zones (Figure 4.2) as identified by Horn, 2021.

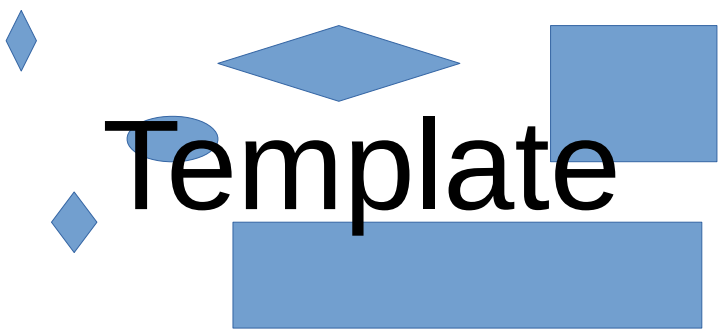


Figure 4.6: Spatial distribution of the in this study considered 650 drinking wells (a) and 5498 irrigation wells. In (b) a distinction between wells from the two different surveys from 2003 (green) and 2015 (red) is made.

Chapter 5

Implementation of the Model

5.1 Implementation of the Model

5.1.1 Modelling Software: GMS

- **About GMS**

- In this study the Groundwater Modeling System (GMS) software by Aquaveo, LLC. is used as modelling environment.
- It is a common software applied in the field of hydraulic, hydrologic and groundwater modelling and is used by many federal and local governmental agencies (Aquaveo, 2021).

- **Basic Functioning**

- Regarding the fundamental flow calculations GMS bases on the modular finite-difference flow model MODFLOW (McDonald and Harbaugh, 1988), which is available in various versions. To simulate seawater intrusion, the three-dimensional multi-species solute transport model MT3DMS (Zheng and Wang, 1999) and the variable-density groundwater flow model SEAWAT (**Langevin.2009**) will be applied in future studies to the here examined model. As SEAWAT bases on MODFLOW-2000 (Harbaugh et al., 2000), in this study this particular MODFLOW version is used.

-

- MODFLOW itself is divided into a series of processes and packages. While major tasks are organised as processes, more specific tasks are executed by packages leading to the eponymous modularisation. Therefore, each optional package provides a different functionality. To utilise these particular functionalities, the corresponding packages need to be activated for the single elements of a GMS model.

-

- In GMS numerical groundwater models are generated either by direct manipulations of a defined three-dimensional grid or by a conceptual modelling approach, as it is applied in this study. For this latter approach GMS utilises common GIS-objects such as points, arcs and polygons which are defined as distinct features on different layers. Each layer represents one homogeneous class of objects - one of the above mentioned feature types - which correspond to one specific term of the groundwater flow equation (Section 5.1.2).

5.1.2 Model Equations

As a basis for future work, in the scope of this study the temporal evolution of a constant-density flow in the Chtouka aquifer is to be considered. The assumption of constant density implies two simplifications of the real world system: First the incompressibility of the flowing medium water, second the neglect of saltwater intrusion. Therewith the groundwater flow in the system that is schematically depicted in Chapter 4 is described by the groundwater flow equation (2.14),

$$S_s \frac{\partial h}{\partial t} = \frac{\partial}{\partial x} \left(K_{xx} \frac{\partial h}{\partial x} \right) + \frac{\partial}{\partial y} \left(K_{yy} \frac{\partial h}{\partial y} \right) + \frac{\partial}{\partial z} \left(K_{zz} \frac{\partial h}{\partial z} \right) + \dot{M}_{ss,i} \quad (5.16)$$

where K_{xx} , K_{yy} and K_{zz} denote the hydraulic conductivities in (m s^{-1}) along the x -, y - and z -axis respectively, h the potentiometric head in (m), S_s the specific storage of the porous medium (m^{-1}) and t the time (s).

$\dot{M}_{ss,i}$ denotes the different source- and sink-terms i as volumetric flux per unit volume (s^{-1}). These are following the conceptual model here the recharge from precipitation, the withdrawal from both drinking and irrigation wells and the irrigation returns. Negative values of $M_{ss,i}$ imply flow out of the system and positive values flow into the system.

As explained in Section 2.2 only the diagonal elements K_{ii} of the hydraulic conductivity tensor are here considered. In the deviation of the equation this is possible due to the arbitrary choice of orientation of the coordinate system in the single control volumes parallel to the major axes of the hydraulic conductivity (Harbaugh et al., 2000). However it may be noted that in MODFLOW-2000 only a global coordinate system is considered. As stated in Section 5.1.4 this coordinate system is oriented along the cardinal directions.

5.1.3 Implementation in GMS

- the geological model

- The geological model used in this study was implemented by Horn (2021) in GMS first as a triangulated irregular network (TIN). It was then discretised as described in Section 5.1.4.
- The material properties of the geological units that are relevant for this study are the hydraulic conductivities K and specific storage S_s , as can be seen from the groundwater flow equation (2.14).
- In this study the hydraulic conductivities are assumed to be horizontally isotropic, $K_{xx} = K_{yy}$, and in vertical direction to have an anisotropy with a factor of 10, $K_{xx} = 10 \cdot K_{zz}$.
- As the geological model represents a simplification of the aquifer, exact values of the named parameters need to be estimated basing on the model's behaviour. This is described in Section 5.2.
- **the other layers**
- The other layers of the conceptual model described in Section ?? are imported as distinct layers into GMS. The different features corresponding to each layer are represented by one of the common GIS-objects, as specified in Table 5.1. The different MODFLOW packages applied to each layer are listed here as well. As GMS can process only non-overlapping polygons in one layer, the over time varying private irrigation perimeters are defined on several layers. Therefore each identified period of constant extents (e.g. 1968-1973, see Section 4.5) is implemented in a single layer, leading to a total of six layers for the private irrigation perimeter. As the public and Tassila perimeters do not overlap, these are assigned to one single, shared layer.

Table 5.1: Overview of the in GMS implemented layers. Each layer is comprised of features of the specified object class and utilises the listed MODFLOW packages.
 (*): The time-dependent areas of the private perimeter are divided by corresponding periods into six layers (Section 5.1.1).

5.1.4 Discretisation

The groundwater flow equation (2.14) is a non-linear, inhomogeneous partial differential equation. Therefore it cannot trivially be solved analytically for the described system. Within the framework of GMS the equation is therefore solved numerically. A three-dimensional cartesian grid is generated and Equation (2.14) is solved on this grid for

defined time steps using the finite difference method. For further details on the solution method refer to Harbaugh et al. (2000).

Spatial Discretisation

- In this study the by Horn, 2021 derived three-dimensional discretised geological model is used
- it bases on an implementation of the original geological model as from which the three dimensional grid was generated using the grid overlay approach in MODFLOW-2000
-
- In horizontal direction the resulting grid has a quadratic cell size of 500 m × 500 m with cell edges oriented in the four cardinal directions. Positive x -direction points to the east, positive y -direction to the north (Figure 4.4).
- In vertical direction, the model is set to a thickness of 10 equally spaced layers with therefore in x - and y -direction locally varying depths. Positive z -direction points upwards. The minimum layer thickness is set to 2.5 m. The top- and bottom-most cell faces are defined as variably shaped surfaces, depending on the DEM and the bottom of the solids. The shapes of the inter-cellular faces are linearly interpolated between the outer two.
- To each cell the lithological unit locally incorporating the largest volume is assigned, defining the cell's material properties.

Temporal Discretisation

- Regarding the temporal discretisation, MODFLOW 2000 utilises a division into stress periods and time steps. Stress periods are generally defined in GMS as periods of constant transient stresses (e.g. pumping rates, precipitation). Each stress period can have a particular length and is further sub-divided into a number of equally long time steps.
- For this model stress periods are defined as the single hydrological years, which start on 1st of September at 00:00:00 of one year and end on 31st of August of the subsequent year at 23:59:59. They therewith show a variable length due to leap years.
- The number of time steps is set to two per stress period. This was initially assumed as sufficient, as
- (Description, why this is sufficient: from theory why this is to be expected, and state that the correctness of this assumption was tested)

- The correctness of this conclusion was successfully tested through comparison of simulations with otherwise constant parameters. Their results showed equality.
- ADD: transient model run with first time step being treated as steady state (more or less), thus giving the stable initial condition for the transient simulation

5.2 Methodology of Sensitivity Analysis and Calibration

The true behaviour T of a system can be either measured, through which an experimental value E is obtained. Or it can be modeled, which yields a modelling value M . In either case, the results obtained deviate from reality due to measuring errors δ_E or modelling errors δ_{SM} (Stern et al., 2001),

$$T = E - \delta_E \quad (5.17)$$

$$T = M - \delta_{SM} \quad (5.18)$$

Although models represent a simplified version of reality, they are often described by complex mathematical equations that cannot be solved analytically. Therefore the exact modelling value M is numerically approximated by a simulation value S . Likewise, this value underlies a numerical error δ_{SN} (Stern et al., 2001),

$$M = S - \delta_{SN} \quad (5.19)$$

The simulation result can be expressed as function f of system inputs (the key variables) \mathbf{X} and parameter combinations $\boldsymbol{\theta}$ (Naeini et al., 2019),

$$S = f(\mathbf{X}, \boldsymbol{\theta}) \quad (5.20)$$

In this study each specific combination $\boldsymbol{\theta} = (\theta_1, \dots, \theta_N)$ of values θ_i of the N different parameters i is called a parameter set. All possible parameter sets constitute the parameter space Θ .

The adequacy of a model for a specific purpose can be assessed through its capability to describe the behaviour of the real system. Thus with Equations (5.18), (5.19) and (5.20) follows:

$$T = f(\mathbf{X}, \boldsymbol{\theta}) - (\delta_{SM} + \delta_{SN}) \quad (5.21)$$

To achieve a close fit of the model to the reality, it is necessary to minimise the numerical and modelling errors. The prior can be decreased among others through the choice of

an adequate discretisation and solution scheme as well as through the refinement of the discretisation. The latter depends on both the modelling function f itself and the choice of a suitable parameter set $\boldsymbol{\theta}$. f is defined through the modelling equations whose exact formulation depends on the conceptual model. Therefore after assembling a model to a state as far as described for the here applied model, a further reduction of the simulation error is only possible through an adjustment of the model parameter values $\boldsymbol{\theta}$.

A model's response significantly depends on these parameters. An example is shown in Figure 5.1. Depending on the choice of the specific parameter set, the modelling error varies. This variation is generally non-linear and can show a great deal of interaction between the different parameters (Duan et al., 1993). Thus within the parameter space Θ not only one global optimum may exist for which the modelling error reaches its global minimum ($\boldsymbol{\theta}_{go}$ corresponding to a point within the green area in Figure 5.1). But there also may be several other local optima at which the modelling error becomes locally minimal. In Figure (Fig-ParamSpaceEx) these are within the closed yellow and orange areas in the top-left, of which one is exemplarily marked corresponding to $\boldsymbol{\theta}_{lo}$.

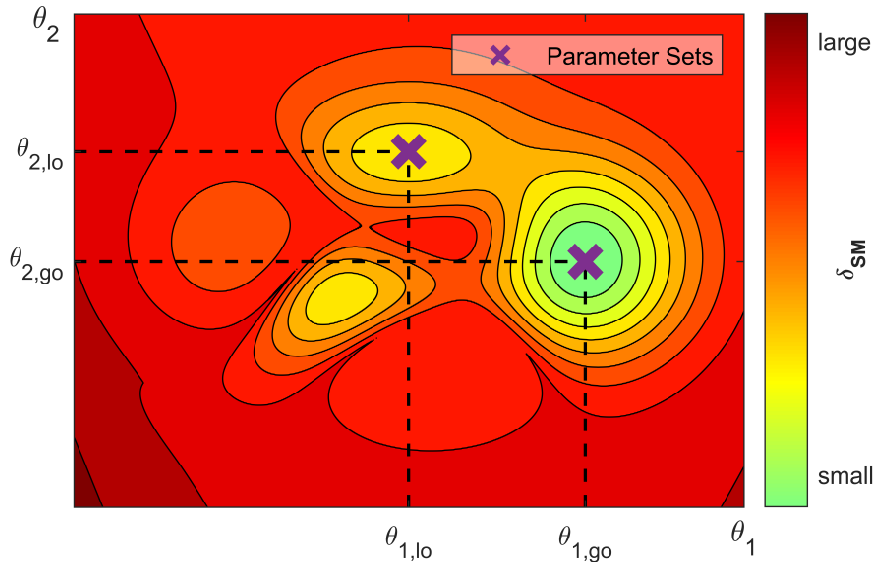


Figure 5.1: Example of a two dimensional continuous parameter space Θ with elements $\boldsymbol{\theta} = (\theta_{1,i}, \theta_{2,j})$. Each of these parameter sets corresponds to an absolute modelling error δ_{SM} marked by the colour scale. In this example, the parameter set $\boldsymbol{\theta}_{lo}$ corresponds to a local minimum of the modelling error δ_{SM} . The global optimum of δ_{SM} is obtained by the parameter set $\boldsymbol{\theta}_{go}$.

The process of finding the parameter set corresponding to the global minimum of δ_{SM} is called calibration. The procedure used in this study is described in Section 5.2.3.

As the function $f(\mathbf{X}, \boldsymbol{\theta})$ is often unknown, calibration needs to be conducted by simple trial-and-error. Therefore it is computationally expensive and if carried out manually

also very time-consuming. However, not all model parameters impact the model results equally extensive (Duan et al., 1993). Therefore, the number of parameters considered in calibration of a model can preliminarily be reduced to only those parameters with significant impact. To identify these different impacts, the behaviour of the model to changes in single parameters is examined in a sensitivity analysis prior to the calibration. The procedure of the sensitivity analysis that this study follows is described in Section 5.2.2.

Crucial to the success of both sensitivity analysis and calibration is the meaningful measurement of the modelling error δ_{SM} . Several different measures exist that have different characteristics. Section 5.2.4 describes the methodology followed in this work.

Prior to sensitivity analysis and calibration however, the examined parameters need to be identified. In this study, not all model parameters are taken into account. Those examined in the sensitivity analysis are described in the following Section 5.2.1.

5.2.1 Examined Parameters

In this study, three groups of parameters are identified for which the model is to be calibrated. Two of these directly follow from the groundwater flow equation (2.14): the hydraulic conductivities K_{ii} and the specific storage S_s . For the third one it is acknowledged that the estimations of the pumping rates underly a large uncertainty. Therefore the associated sink-term $\dot{M}_{ss,irr}$ is provided with a scaling factor $\theta_{Q,irr}$.

Both the hydraulic conductivities and the specific storages are material properties and characterise the geological model for the flow model. Therefore, both have specific values for each of the five lithological units into which the model is divided. Although each of the parameters therewith corresponds to a defined unit, exact values are unknown. This is due to the coarse classification into five lithological units of the possibly more heterogeneous geology of the aquifer. Likewise, characterisations in literature differ.

A within the project framework conducted literature research identified for hydraulic conductivities a range of values over several orders for each material. The corresponding minimum and maximum values are listed in Table 5.2.1. Therewith no direct specification between the hydraulic conductivities in x -, y - and z -direction are possible. To reduce the dimensions of the parameter space, certain assumptions are made. First, as the flow directions in the xy -plane vary in space while no location-dependent variation of K_{xx} and K_{yy} is possible within the model framework, a horizontal isotropy is assumed,

$$K_h = K_{xx} = K_{yy} \quad (5.22)$$

where K_h is the horizontal hydraulic conductivity. Second, a constant anisotropy between horizontal and vertical hydraulic conductivity is assumed with a proportionality factor of 10,

$$K_h = 10 K_v = 10 K_{zz} \quad (5.23)$$

with the vertical hydraulic conductivity K_v . In the following the hydraulic conductivities will be expressed in terms of the horizontal hydraulic conductivities $K_h^{(i)}$ of the materials i .

In the same, prior to this study conducted literature research it was found that few values for the specific storage are available in literature. Therefore, more data concerning the specific yield and the effective porosity of probes is given. Thus, the values for the specific storage are approximated with Equation (2.7) through the specific yield S_y and the aquifer thickness b . Values for the specific yield can either be measured directly or approximated as equalling the effective porosity of a probe. The identified range of values for these two quantities are shown in Table 5.2.1. The aquifer thicknesses b refer to average thicknesses of the respective lithological units. However, these thicknesses are not constant but vary significantly in space. To account for this the geological model is examined statistically. From this analysis ranges of the material thicknesses are estimated. The corresponding limits are defined by the 20%- and 80%-Quantiles (Figure ??, Table 5.2.1). From these estimations of S_y and b the ranges of values for the material-specific specific storages are calculated as described. The results are shown in Table 5.2.1. In the following the specific storages will be expressed as $S_s^{(i)}$ of the materials i .

Table 5.2: Overview of the value ranges of the parameters horizontal hydraulic conductivity K_h and specific storage S_s for all materials. Furthermore the value ranges of specific yield S_y and material thickness b are listed that were used to calculate the specific storages.

Material	K_h (m s^{-1})		S_y (-)		b (m)		S_s (m^{-1})	
Calc. Marl	$1 \cdot 10^{-6}$	$1 \cdot 10^{-4}$	23	38	21	109	$2 \cdot 10^{-3}$	$2 \cdot 10^{-2}$
Gravel	$1 \cdot 10^{-7}$	$9 \cdot 10^{-5}$	2	10	20	85	$2 \cdot 10^{-4}$	$4 \cdot 10^{-3}$
Sand	$8 \cdot 10^{-5}$	$1 \cdot 10^{-2}$	17	24	13	54	$3 \cdot 10^{-3}$	$2 \cdot 10^{-2}$
Silty Sand	$1 \cdot 10^{-7}$	$1 \cdot 10^{-3}$	10	40	32	350	$3 \cdot 10^{-4}$	$1 \cdot 10^{-2}$
Gravel	$4 \cdot 10^{-7}$	$5 \cdot 10^{-4}$	1	26	23	140	$7 \cdot 10^{-5}$	$1 \cdot 10^{-2}$

Regarding the uncertainties of the pumping rates of the irrigation wells, prior to this study an expert on plant hydrology was consulted. An assessment was done on how realistic the yearly withdrawn water volumes might be. The estimations base on the expectable evapotranspiration when taking into account the irrigated area and cultivated plant species. As result, an underestimation of water withdrawal volumes by a factor of 2 was deemed possible. Thus, the range of values for the scaling factor of the irrigation flow rate is set to an interval of

$$\theta_{Q,irr} = [0.5, 2.0] \quad (5.24)$$

In total, a parameter set $\boldsymbol{\theta}$ therewith comprises of five values of hydraulic conductivities, five values of specific storages and one value of the scaling factor $\theta_{Q,irr}$ of the irrigation flow rate. The parameter space is accordingly 11-dimensional.

5.2.2 Methodology of the Sensitivity Analysis

- For the sensitivity analysis a reference basic parameter set $\boldsymbol{\theta}_3$ is picked which
- to examine the model's behaviour in respect to the different parameters, each parameter is varied separately in respect to this parameter set within its defined ranges
- the model's behaviour to changes of this single parameter within the defined parameter set is assumed as being representative also for other parameter sets
- therefore the underlying parameter set is chosen to represent average values of the parameters and not extreme values
- thus, $\boldsymbol{\theta}_3$ is defined as the geometric averages of the different parameters
- in this study, the model's response S is evaluated for five values of each parameter
- the hydraulic conductivities and specific storages from Table 5.2.1 often range over several orders
- therefore a logarithmic partition of the defined intervals is applied with constant proportionalities between neighbouring values
- accordingly, the middle value $\theta_{i,3}$ of parameter i denotes the geometrical average
- the set of the five examined values $\theta_{i,1}, \dots, \theta_{i,5}$ is defined by
- (Equation)
- where n is the number of values, thus $n = 5$.
- the response S of the model is measured through analysis of the dependent variable head h , as described in Section 5.2.4
-

$$\bigcup_{j=1,\dots,n} \theta_{i,j} : \theta_{i,j} = \left(\frac{\text{Max}(\Theta^{(i)})}{\text{Min}(\Theta^{(i)})} \right)^{\frac{j-1}{n-1}} \cdot \text{Min}(\Theta^{(i)}) \quad (5.25)$$

5.2.3 Methodology of the Calibration

- **Generals**
 - the goal of the calibration is to identify a parameter set $\boldsymbol{\theta}$ that globally minimises the modelling error δ_{SM}
 -
 - **optimisation problem:**
 - global optimisation
 - several major areas to which a search strategy may converge (Duan et al., 1993)
 - within these areas possibly numerous local optima both close to and at various distances from the best solution (Duan et al., 1993)
 - the parameters may show a great deal of (possibly non-linear) interaction and compensation (Duan et al., 1993)
 - feasible parameter space Ω (Duan et al., 1993)
 - start of search requires large enough number of points to identify major regions of attraction (Duan et al., 1993)
 - followed by clustering in most promising regions (Duan et al., 1993)
 - though clustering may not be too focussed to sustain robustness of the search against local optima
 - **Description of Calibration Process/Algorithm**
 - in this work, calibration is conducted manually.
 - both the changing of the parameter values on each simulation run and the corresponding evaluation of the model's results
 - manually executed algorithm
 - goal is to find the global optimum
 - therefore several loops of iterations are done; each loop comprises of one cycle over all parameters of one parameter class (hydraulic conductivity K or specific storage S_s);
 - for each parameter i an interval $X^{(i)} = [\text{Min}(X^{(i)}) \text{ Max}(X^{(i)})]$ is specified within each iteration; from this interval $n = 5$ or $n = 7$, on a logarithmic scale equally spaced values $x_j^{(i)}$ as described before in Section 5.2.2 and Equation (5.25)
 - a

- This describes the ideal process for calibration. However, in this study it is not strictly followed as during the calibration process the parameter ranges were repeatedly adjusted for various reasons. Nonetheless the here described schematic was used as coarse guideline and orientation

5.2.4 Error Assessment

- common measures for error estimation are the root mean square error ($RMSE$) and the mean absolute error (MAE)
- these average single errors $y_i - \hat{y}_i$ between a measurement value y_i and a reference value \hat{y}_i over all n instances i through different averaging methods
- $RMSE$ and MAE are defined by

$$RMSE = \sqrt{\sum_{i=1}^n \frac{(y_i - \hat{y}_i)^2}{n}} \quad (5.26)$$

$$MAE = \frac{\sum_{i=1}^n |y_i - \hat{y}_i|}{n} \quad (5.27)$$

- The mean absolute error therewith represents the arithmetic average of the single errors $y_i - \hat{y}_i$, thus giving each error the same weight on a linear scale.
- The $RMSE$ on the other hand, as it first squares the single errors, weights larger errors higher than smaller errors.
- In the previous study by Horn (2021), the error of the model was estimated through these two measures
- therefore the spatially distributed measuring points were regarded as an ensemble. Thus the underlying 3-dimensional continuous scale holding the spatial information could be reduced to a 1-dimensional nominal scale, with the identifier being the piezometer name.
- therewith an average response of the model - where the aquifer is regarded as a unit - to changes in parameter values could be estimated
- in this study however, the model is regarded in transient state.
- this introduces an additional dimension, the time
- this dimension's scale, as it is discrete and not nominal, holds information about correlations between the values
- trivially, values at later times depend on values at preceding times

- using one of the aforementioned error measures thus leads to loss of information about these dependencies, since every point in time is regarded as an independent instance
- this issue is illustrated in Figure 5.2 (a)
- all three simulations have the same *RMSE* in comparison to the observation time series, but their temporal evolution deviates significantly from each other
- Simulation 1 shows no time dependent behaviour at all.
- In case of Simulation 2 the long-term trend matches that of the observation. However, the results underly an offset in head.
- In case of Simulation 3 the initial offset is even larger, diminishes until the end of the measuring period due to an underestimation of the long-term trend.
- An error analysis using the *RMSE* could not distinguish between these different cases.
- However, depending on the application the different behaviours may be suitable in different ways.
- Therefore, the *RMSE* and the *MAE* - for analogue reasons - are deemed unfit for the assessment of time series data as in this study.
- To derive a more adequate measuring method the correlation between the observed dependent variable and the simulated dependent variable are considered. In Figure 5.2 this is illustrated for the here used dependent variable head h .
- As basis, it is assumed that a correlation between these two exists and that it can be approximated as linear relationship.
- Therewith it can be parametrised through linear regression,

$$S \approx p_0 + p_1 E \quad (5.28)$$

- with the regression coefficients p_0 and p_1 .
- (shown in figure)
- p_1 denotes the slope of the curve;
- For determination of the coefficients, least-squares fitting is applied in this study. Therewith, values in proximity to the limits affect the choice of p_1 with a higher weight, as in these regions the residuals are more sensitive to the coefficient.

- under the assumption that short-term fluctuations of hydraulic head in an aquifer are of significantly smaller amplitude than long-term trends, this coefficient is primarily affected by the latter. Thus, p_1 can be understood as comparing the long-term trends of simulation S and observation E with each other. Values $p_1 \approx 1$ denote a similar representation of the trends from the observations by the simulation. Values $p_1 > 1$ or $0 < p_1 < 1$ indicate an overestimation or an underestimation of the observed trend, respectively. Values $p_1 < 0$ denote an under- or overestimation of the trend, but in opposite direction - e.g. while in the observed time series a drawdown of hydraulic head exists, the simulation results would give an increase in hydraulic head.
- To estimate long-term trends from observational data, observations need to cover sufficiently long time periods. In this study, only time series covering 7 or more years are considered for estimation of p_1 . Furthermore, as at four locations a respective pair of piezometers is covering separate time periods (Section 4.6), their time series are merged pairwise. To account for the higher certainty at these locations, each piezometer is in the evaluation still considered a single independent observation point, but with the merged time series. This gives each of the piezometer pairs a doubled weight in respect to the other piezometers.
-
- p_0 denotes the intercept of the fitted curve with the y -axis of the correlation plot. In this application it marks therewith the simulation value that would occur for an observation value $E = 0$. Such a value however may not be reached in the described, real system, and thus p_0 is a primarily mathematical quantity. Furthermore, p_0 highly depends on the interval of simulation values and empirical values that are compared. For intervals over large observation values of exclusively the same sign, small changes in p_1 result in significant changes of p_0 . Also, each measuring location may have an individual observation error δ_E . For the aforementioned issues however, this error cannot directly be incorporated into p_0 .
- To overcome these issues, a standardisation in respect to the actual values of S and E is necessary. As in this study time series are regarded, the initial offset

$$\Delta S_0 = T(t=0) - S(t=0) \quad (5.29)$$

- is chosen as representation of the true parallel shift between the truth T and the simulation S at time $t = 0$. However, in this study only 8 out of 27 available observation time series date back to the here chosen initial date, the year 1968. To still enable the assessment of the other time series in respect to this characteristic, values are extrapolated for $T(t=0)$ in the affected cases. Therefore the assumption is made that the modeled trends sufficiently correlate to the observed trends. To obtain an expression for $T(t=0)$, Equation (5.28) can first be written for $t = 0$ as

$$S(t=0) = p_0 + p_1 \cdot E(t=0) \quad (5.30)$$

Solving for $E(t = 0)$ yields

$$E(t=0) = \frac{S(t=0) - p_0}{p_1}$$

Together with Equation (5.17), Equation (5.2.4) can thus be written as

$$\Delta S_0 = \frac{S(t=0) - p_0}{p_1} - \delta_E - S(t=0)$$

rewriting finally yields

$$\Delta S_0 = S(t=0) \cdot \left(\frac{1}{p_1} - 1 \right) - \frac{p_0}{p_1} - \delta_E \quad (5.31)$$

As ΔS_0 depends on $1/p_1$, it may be noted that ΔS_0 is only defined for values $p \neq 0$.

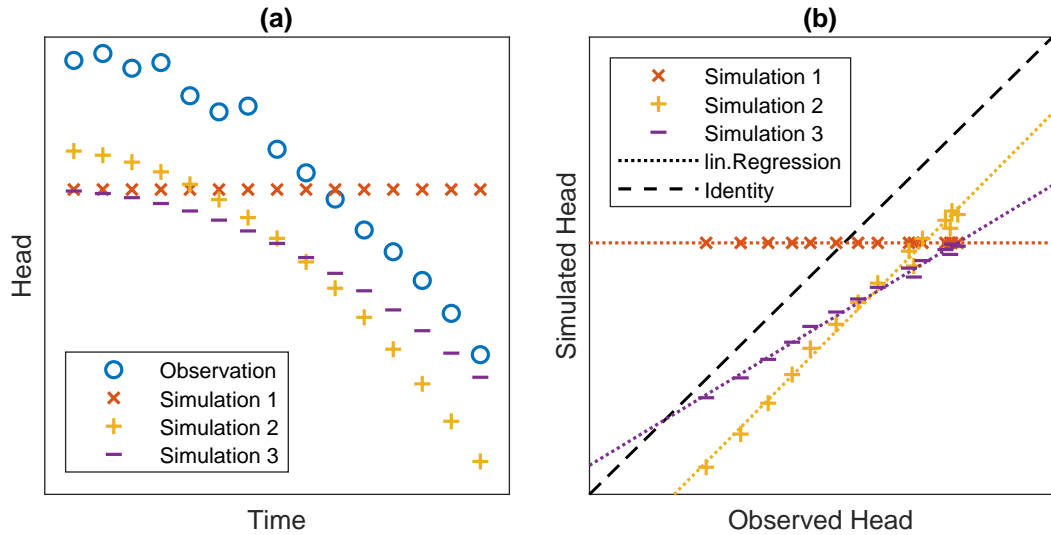


Figure 5.2: (a): Time series of an observation and of three simulations with different parameter sets. In comparison with the observation all three simulations have an equal $RMSE$. (b): Linear representation of the correlations between observed and simulated heads for the three simulations from (a). The respective data sets are each fitted with a linear (lin.) regression. The black dashed line marks identity between observed and simulated head.

for error quantification

Derivation of new Error Measure

comparison between simulation and truth (or measurement) leads to correlation to assign somewhere:

- analysis of model properties for estimation of range of values of specific storativity -*i*, this goes to the section preceding sensitivity analysis and calibration, as here-with model properties are examined to determine value ranges for the named two investigations
-
- aaa

Derivation of p_0 and p'_0

- δ_E is considered here, as it will be incorporated into p'_0 (not really into p'_0 itself, but into its graphical presentation; this is necessary as we have different δ_E depending on the location, which cannot be resolved due to the nominal consideration of the different piezometers (not really true, the piezometers do not have a spatial correlation between δ_E and location)); this would also not be possible with only p_0 due to the lack of physical meaning of it
- the goal of the calibration is to identify a parameter set $\boldsymbol{\theta}$ that minimises the modelling error δ_{SM} as defined in Equation (5.18)
- however, a comparison of the simulation result S to the truth T as in Equation (5.21) is not possible, since T is unknown
- S can therefore only be compared either to other simulations' results or to measured values E
- in this study, the latter approach is applied
- from Equations (5.17) and (5.21) follows

$$E = f(\mathbf{X}, \boldsymbol{\theta}) - (\delta_{SM} + \delta_{SN}) + \delta_E \quad (5.32)$$

- therefore also the measuring error needs to be considered
- it needs to be kept in mind that the truth however is unknown and only approximated by experimental results/values, which in this study are the observations of the key variable hydraulic head h
- relevant of this in the context of this work is, that the simulation values S are compared to the measurement (and thus to experimental) values E , not the truth T ; accordingly $E = S - (\delta_{SM} + \delta_{SN}) + \delta_E$ with $\delta_E = E - T$

Chapter 6

Results

6.1 Discussion of Error Measure

alternatives would be to use the difference between a possible over a few years/time units time-averaged RMSE at the start and at the end of the simulation/calibration period; therewith however possible developments in between would not be captured; in case of this study - as the results show - this would not be a significant issue, as most wells only show a monotonic behaviour

the simulations accuracy considering non-monotonic behaviour over time can also be captured through the error assessment technique, also here each value in time is compared between simulation and measurement; thus

comparison to other error measures: - gives additional information (so far two measures, could be extended to three (R^2)) while using the same data basis - computationally more expensive, as a linear regression needs to be conducted for each observation location; however it is not examined how this scales up for increasing measuring locations; it can however be assumed for most applications the main driver of computational costs is the execution of the simulations, not the mathematical analysis of the results - initial implementation is more laborious; though for the experienced programmer should not take a significant amount of additional time, compared to the RMSE for example; plus once implemented, the corresponding script can be applied to other models as well - assumption in derivation, that correlation between simulation values S and observations E exists should be legitimate, as the goal of a model is to reproduce observations (or at least certain characteristics of them) - in the derivation of ΔS_0 the assumption is made that a sufficient correlation between observed (and true) trends and simulated trends exists. This assumption should well be legitimate, as the goal of a model is to reproduce such trends and therefore the model should accordingly be designed. Furthermore, the correctness of this assumption can be assessed through the coefficient of determination R^2 of the applied linear regression. - for fluctuations/scattering two main sources are thinkable: measuring errors and intermittent(?) behaviour that is not yet sufficiently accounted for through the model - the verification/validation of ΔS_0 is yet to be done (maybe put into the conclusion)

6.2 Sensitivity Analysis

Recapitulation:

- the sensitivity we estimate here as shown in the short formula as the root mean squared error between the simulated heads for the Q5 and Q95 parameters
-

last time we presented only preliminary results

therefore here are now the updated results:

- the sensitivities to the single parameters are location-dependent
- _____
- for the specific storage we found that only three geological units have a major impact
- these units are the Marly-calcareous sediments, Sand and Schist
- in the bottom here we see a comparison, how big the sensitivities are at the single piezometers
- _____
- for the hydraulic conductivity, a sensitivity analysis was already done for the steady state model
- however in transient mode, it can have different impacts, so we carried out another sensitivity analysis for it as well
- the results are that four out of five geological units have a high impact on the simulation result
- only Silty Sand does not need to be considered here
- as we can see from the two examples shown down here, also other areas are affected by changing the hydraulic conductivity than for the specific storage
- _____
- additional to this, we examined the sensitivity to one more parameter
- as we have some uncertainties regarding the pumping rates, we also varied it
- as lowest pumping rate we used the original one
- as highest pumping rate we used one three times higher
- as was to be expected, the model is also sensitive to these

- also the sensitivity depends on the location, and we have the highest effect in the private and public irrigation perimeters
- _____

(Eastern Boundary adjusted)

2 slides

here we have the summary of the sensitivity analysis

- all in all, the model behaves sensitive not to all material-specific parameters and not at all piezometers
- as we can see here, piezometers close to the west and south boundaries are only little affected by them
- for the main irrigation area they are more important
- so all in all we can reduce the further considerations to fewer parameters and fewer piezometers

therewith we can come to the next step in the modelling, the calibration of the model through the important parameters

Notes on Presentation of Results

- the results of the sensitivity analysis have been initially shown through plots of the RMSE for each piezometer
- as argued under Section ??, this approach is not representative for time series
- therefore, for the sensitivity analysis the usage of the coefficients of linear regressions to the correlations between observations and simulation results might also be reasonable
- for presentation in the thesis, the current (many) plots are of no use
- first of, the goals of the sensitivity analysis:
 - a identification of relevant parameters
 - b identification of relevant piezometers
 - c ... others?
- for revision, the following approaches might be useful:
 - b1 one possibility would be to use boxplots:
 - * x-axis:
the single piezometers,

* y-axis:

- the p_0 :
heads or (maybe relative) changes of heads
- p_1 :
logarithmic scale because of nature of this coefficient (but here problem of handling negative values, which would require an additional tile)
Handling of negative values:
Partition of values into two graphs:
one of two tiles per positive and negative values;
here, somehow the information on constitution of number of positive (negative) values each should be added somewhere in the graph, as these can vary;
possibility: colouring of boxes, depending on number of negative values - seemingly so far only 5 max
- R^2 :
if once working properly, this can show which piezometers are affected by higher non-linearities or fluctuations, and if these can be influenced by parameter changes

→ tiled layout (3,1)

- * the samples for each piezometer:
the - either global or parameter-specific - linear regression-results of the single simulations;

• a

6.2.1 Calibration

text and *text* is used.

Goodness of Fit Assessment

Motivation:

- in the previous study, the model has been calibrated for the steady state
- in steady state, at each sampling/observation point (piezometer) the simulation result is one single value

- this value can directly be compared with the observation, yielding the local error
 - e.g. through a simple difference between both values
- for a global error estimate, these local errors have been summarised using the mean average error (MAE) and root mean squared error (RMSE)
- however, in transient state at the single observation points both observations and simulation results are each a time series
- as the values of the heads are time-variant, so can be the deviations (errors) between them, introducing an additional degree of freedom into the system
- using the MAE or RMSE to locally summarise the error over each time series at each piezometer does therefore not yield an unique error estimate
- in Fig. 6.1 three different possible simulation results are shown, all of which having an equal RMSE over their time series in comparison to the observations
- therefore, a different measure is required to assess the goodness-of-fit that a parameter set yields

Description of new Method:

- for an alternative measure, the correlation between the observations and the simulation results can be regarded
- herefore, each single simulation result is compared to the corresponding observation at the same time
- if the simulated results all have the exact same values as the observations (and different values are observed), all points lie on a line of slope and that intercepts the axes at [0 0]
- the correlation between observations and a specific simulation's results can be characterised through a linear regression (linear correlation)
- this regression yields two coefficients: the slope p_1 and the intercept p_0
- for these coefficients, the calibration goal can be determined as: $p_1 \approx 1$ and $p_0 \approx 0$
- however, this characterisation presumes a strict linear correlation between observations and simulation results (which would apply in the ideal case of *simulation = observation*)
- in real, such a relation does not appear - due to different behaviour of the model and due to measuring errors of the observations
- to characterise this non-linearity of the correlation (the deviation from the presumed linear correlation), the coefficient of determination R^2 of each linear regression can be calculated

- values close to 1 indicate a strong linear correlation, whereas values $\ll 1$, ≈ 0 indicate high variance

$$f_{vD}(x) = a \sin\left(\frac{2\pi}{k}(x - x_0)\right) + y_0 \quad | \quad x \in [x_{min}, x_{max}] \quad (6.33)$$

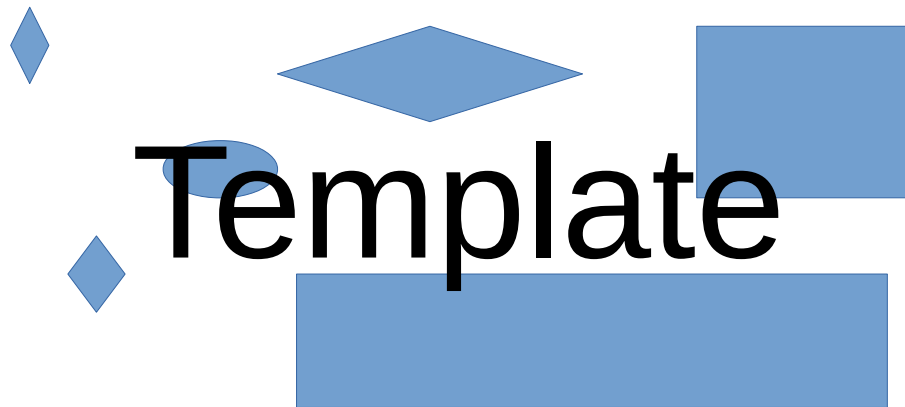


Figure 6.1: Figure example.

1-1-2

6.2.2 1-2

blablabla

new page

6.3 2

6.3.1 2-1

2-1-1

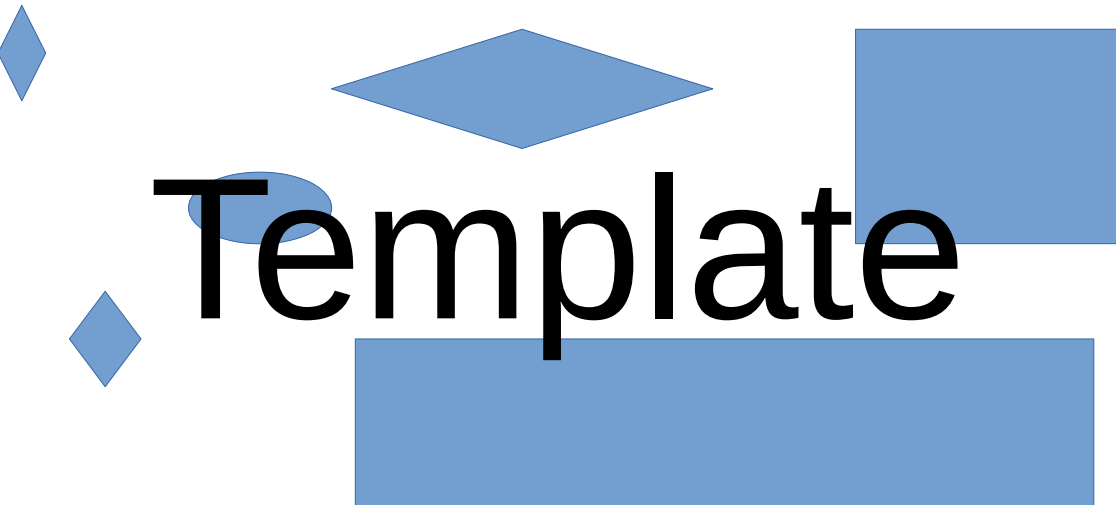


Figure 6.2: Figure Example.

$$\xi_i^* = \begin{cases} \xi_0 & |i = 1 \\ c_\xi (\xi_{i-1} + n_{i-1}) + (1 - c_\xi) \xi_0 & |i > 1 \end{cases} \quad (6.34)$$

Here $c_\xi = 1$ denotes the application of a continuous relief, while $c_\xi = 0$ establishes individual phase offsets, leading to a possibly discontinuous relief.

Chapter 7

Summary and Discussion

hi.

aaaaa

Bibliography

- Agence du Bassin Hydraulique de Souss Massa (2022). *Etat de remplissage des retenues de barrages 07/09/2022 à 08h00*. Webpage. Accessed: 13.09.2022. Agence du Bassin Hydraulique de Souss Massa. URL: www.abhsm.ma.
- Agence du Bassin Hydraulique de Souss Massa et Drâa (2005). *Stratégie de préservation des ressources en eau souterraine dans le bassin du Souss Massa - Plan d'action 2005-2020*. Tech. rep. No public access, information as cited in (Choukr-Allah, Nghira, Hirich and Bouchaou, 2017), p. 61.
- (2014). *Eau Souterraine: Evaluation des eaux*. Webpage. Accessed: 17.09.2022. URL: www.abhsm.ma.
- (2015). *Etude et élaboration de contrat de nappe de Chtouka (province Chtouka-Aït Baha) Mission 2: Etat des lieux, tendance d'évolution future et élaboration du plan d'action*. Tech. rep. No public access, information as cited in (Malki, Bouchaou, Hirich, Brahim and Choukr-Allah, 2017).
- (2022). *Situation Hydrologique*. Webpage. Accessed: 20.09.2022. URL: www.abhsm.ma/index.php/partenariat-5/situation-hydrologique.
- ANZAR CONSEIL (2016). *Etude et élaboration de contrat de nappe de Chtouka - BdD "Prélèvements Nappe Chtouka"*. Tech. rep. No public access, information as cited in provided project data.
- Aquaveo, LLC. (2019). *GMS:Conductance*. Accessed: 13.09.2022. URL: www.xmswiki.com/wiki/GMS:Conductance.
- (2021). *Aquaveo Webpage*. Accessed: 06.09.2022. URL: www.aquaveo.com/.
- Bernet, G. and A. El Habil (1977). “Plaine de Chtouka”. In: *Ressources en Eau du Maroc, Tome 3: domaine atlasique et sud-atlasique*. Notes et Mémoires du Service Géologique du Maroc 231, pp. 202–211.
- Choubert, G. (1964). *Histoire géologique du Précambrien de l'Anti-Atlas*. 162. Éditions du Service géologique du Maroc.
- Choukr-Allah, R., A. Nghira, A. Hirich and L. Bouchaou (2017). “Water Resources Master Plan for Sustainable Development of the Souss-Massa River Basin”. In: *The Souss-Massa River Basin, Morocco*. Ed. by R. Choukr-Allah, R. Ragab, L. Bouchaou and D. Barceló. Springer.
- Critchfield, H. (1983). *General Climatology*. 4th ed., p. 453.
- Direction Régionale de Souss Massa (2020). *Annuaire Statistique Régional Souss Massa - 2020*. Tech. rep. Accessed: 18.09.2022. Haut-Commissariat au Plan. URL: www.hcp.ma/region-agadir/.

- Duan, Q., V. K. Gupta and S. Sorooshian (1993). "Shuffled complex evolution approach for effective and efficient global minimization". In: *Journal of optimization theory and applications* 76.3, pp. 501–521.
- English, M. (1990). "Deficit irrigation. I: Analytical framework". In: *Journal of irrigation and drainage engineering* 116.3, pp. 399–412.
- Fetter, C. W. (2001). *Applied Hydrogeology*. 4th ed. Pearson Education International.
- Harbaugh, A. W., E. R. Banta, M. C. Hill and M. G. McDonald (2000). *MODFLOW-2000, The U.S. Geological Survey modular Ground-Water Model - User Guide to Modularization Concepts and the Ground-Water Flow Process*. Tech. rep. U.S. Geological Survey.
- Horn, F. (2021). "Numerical Modelling of Seawater Intrusion in the Chtouka Aquifer, Morocco". MA thesis. Institute of Applied Geosciences, Karlsruhe Institute of Technology.
- Hssaisoune, M., S. Boutaleb, M. Benssaou, B. Bouakkaz and L. Bouchaou (2017). "Physical Geography, Geology, and Water Resource Availability of the Souss-Massa River Basin". In: *The Souss-Massa River Basin, Morocco*. Ed. by R. Choukr-Allah, R. Ragab, L. Bouchaou and D. Barceló. Springer.
- Johnson, A. I. (1967). *Specific yield: compilation of specific yields for various materials*. 1662. US Government Printing Office.
- Krimissa, S., J.-L. Michelot, L. Bouchaou, J. Mudry and Y. Hsissou (2004). "Sur l'origine par altération du substratum schisteux de la minéralisation chlorurée des eaux d'une nappe côtière sous climat semi-aride (Chtouka-Massa, Maroc)". In: *Comptes Rendus Geoscience* 336.15, pp. 1363–1369.
- Malki, M., L. Bouchaou, A. Hirich, Y. A. Brahim and R. Choukr-Allah (2017). "Impact of agricultural practices on groundwater quality in intensive irrigated area of Chtouka-Massa, Morocco". In: *Science of the Total Environment* 574, pp. 760–770.
- Matsuura, K. and C. J. Willmott (2018a). *Terrestrial Air Temperature: 1900-2017 Gridded Monthly Time Series (Version 5.01)*. Accessed 16.09.2022. Department of Geography, University of Newark. URL: http://climate.geog.udel.edu/~climate/html_pages/download.html#T2017.
- (2018b). *Terrestrial Precipitation: 1900-2017 Gridded Monthly Time Series (Version 5.01)*. Accessed 16.09.2022. Department of Geography, University of Newark. URL: http://climate.geog.udel.edu/~climate/html_pages/download.html#T2017.
- McDonald, M. G. and A. W. Harbaugh (1988). *A modular three-dimensional finite-difference ground-water flow model*. U.S. Geological Survey.
- McFadden, L., M. Eppes, A. Gillespie and B. Hallet (2005). "Physical weathering in arid landscapes due to diurnal variation in the direction of solar heating". In: *Geological Society of America Bulletin* 117.1-2, pp. 161–173.
- Ministère de l'Agriculture, de la Pêche Maritime, du Développement Rural et des Eaux et Forêts (2021). *Le Plan Maroc Vert, Bilan et Impacts*. Tech. rep.
- Naeini, M. R., B. Analui, H. V. Gupta, Q. Duan and S. Sorooshian (2019). "Three decades of the Shuffled Complex Evolution (SCE-UA) optimization algorithm: Review and applications". In: *Scientia Iranica* 26.4, pp. 2015–2031.

- NASA Jet Propulsion Laboratory (2013). *NASA Shuttle Radar Topography Mission (SRTM) 1 Arc-Second Global*. Accessed 07.09.2022. NASA EOSDIS Land Processes DAAC. doi: /10.5066/F7PR7TFT.
- Office Regional de Mise en Valeur Agricole de Souss-Massa (2015). *Production Agricole de la zone d'action de l'ORMVASM, année 2014-2015*. Tech. rep. No public access, information as cited in (Malki, Bouchaou, Hirich, Brahim and Choukr-Allah, 2017).
- Resing (2003). *Etude de la stratégie de gestion des ressources en eau dans le bassin du Souss Massa - Mission 1: Diagnostic de la situation actuelle de la gestion et de l'usage des ressources en eau*. Tech. rep. No public access, information as cited in provided project data.
- Schreiber, H., S. Oumarou Danni, A. Touab, F. Abourig, N. Montcoudiol, Y. Ez-Zaouy, M. Hssaisoune and L. Bouchaou (2021). "Study of water salinity in the Chtouka plain (Morocco) using TEM geophysical method, chemical and isotopes tracers". In: *EGU General Assembly Conference Abstracts*, EGU21-12074.
- Schütze, N., S. Kloss, F. Lennartz, A. Al Bakri and G. H. Schmitz (2012). "Optimal planning and operation of irrigation systems under water resource constraints in Oman considering climatic uncertainty". In: *Environmental Earth Sciences* 65.5, pp. 1511–1521.
- Stern, F., R. V. Wilson, H. W. Coleman and E. G. Paterson (2001). "Comprehensive approach to verification and validation of CFD simulations—part 1: methodology and procedures". In: *J. Fluids Eng.* 123.4, pp. 793–802.
- Todd, D. K. and L. W. Mays (2005). *Groundwater hydrology*. 3rd ed. John Wiley & Sons.
- U.S. Geological Survey (2018). *Earth Explorer*. Accessed 07.09.2022. Earth Resources Observation and Science (EROS) Center, USGS. url: <https://earthexplorer.usgs.gov/>.
- Zheng, C. and P. P. Wang (1999). "MT3DMS: a modular three-dimensional multispecies transport model for simulation of advection, dispersion, and chemical reactions of contaminants in groundwater systems; documentation and user's guide". In.

Appendix A

Task of the Master Thesis

Masterarbeit

Numerical investigation of transient water flow in the Chtouka Aquifer, Morocco

Betreuer: Dr. Nelly Montcoudiol (BGR); nelly.montcoudiol@bgr.de

Erstprüfer: Prof. Dr. Thomas GRAF (ISU); graf@hydromech.uni-hannover.de

Zweitprüfer: NN

Background Seawater intrusion is a worldwide phenomenon naturally occurring in coastal aquifers due to the density difference between seawater and freshwater. However, groundwater pumping can induce a landward movement of the freshwater-saltwater interface, which may lead to an increased salinity of the pumped water. In Morocco, the Chtouka region is a major producer of fruits and vegetables intended for exportation. This is only possible through irrigated agriculture and a combined use of surface water and groundwater resources. Intense pumping in the Chtouka aquifer is responsible for the observed water table decline, which exacerbates seawater intrusion and threatens freshwater resources. A recent geophysical survey detected seawater intrusion up to 2.5 kilometers inland. In the near future, water demand is expected to increase due to population growth, increased demand for irrigation and climate change. Consequently, seawater intrusion may move further inland. To investigate the behavior of the seawater intrusion in the Chtouka aquifer, a numerical model was developed using the SEAWAT code (within the GMS software). This model builds on previous existing models and incorporates newly acquired data. As of now, the model has only been calibrated under steady state conditions.

Objectives In this project, water fluxes shall be simulated numerically under transient conditions. The transient model includes pumping rates in the area, irrigation return flow, and rainfall. The numerical code SEAWAT (with the GMS software) will be used. In particular, the following aims shall be accomplished:

1. Literature review of the current state of knowledge in this field.
2. Build a transient variable-density 3D flow model for the time 1969-2020. Also build a constant-density flow model without seawater intrusion.
 - 2.1. Impose transient BC (pumping, rainfall, irrigation from recharge).
 - 2.2. Evaluate the impact of the choice of flux along the Eastern Neumann boundary.

- 2.3. Evaluate the impact of the choice of the Southern BC (Cauchy vs. Dirichlet).
 - 2.4. Develop a strategy to quantify existing pumping rates in extraction wells. Verify if groundwater wells can be lumped or need to be imposed point-wise.
 - 2.5. Calibrate the constant-density flow model with existing head measurements.
3. Compare the variable-density flow model with the constant-density flow model.
 - 3.1. Verify the impact of seawater intrusion on the water levels near the coast: Is the variable-density (or constant-density) model adequately reproducing the water level variations in the piezometers near the coast?
 - 3.2. Verify if the results from the variable-density flow model are in agreement with the observed data from subsurface monitoring devices (SMD) and geophysics surveys (TEM).
 - 3.3. Adjust the calibration of the variable-density flow model accordingly

The following additional aims are also anticipated:

4. Generate scenarios (of climatic change and of future water use) in collaboration with the ABHSM, the local partner. Which scenarios to be co-developed will depend on ABHSM interests and data availability.
5. Evaluate their impact on the availability of freshwater resources in the future (water fluxes, seawater intrusion).